

The Mid-IR and X-ray Selected QSO Luminosity Function

R.J. Assef¹, C.S. Kochanek¹, M.L.N. Ashby², M. Brodwin^{2,3}, M.J.I. Brown⁴, R. Cool⁵,
W. Forman², A.H. Gonzalez⁶, R.C. Hickox^{2,7}, B.T. Jannuzi⁸, C. Jones², E. Le Floch⁹,
J. Moustakas¹⁰, S.S. Murray², D. Stern¹¹

ABSTRACT

We present the J -band luminosity function of 1838 mid-infrared and X-ray selected AGNs in the redshift range $0 < z < 5.85$. These luminosity functions are constructed by combining the deep multi-wavelength broad-band observations from the UV to the mid-IR of the NDWFS Boötes field with the X-ray observations of the XBoötes survey and the spectroscopic observations of the same field by AGES. Our sample is primarily composed of IRAC-selected AGNs, targeted using modifications of the Stern et al. (2005) criteria, complemented by MIPS $24\mu\text{m}$ and X-ray selected AGNs to alleviate the biases of IRAC mid-IR selection against $z \sim 4.5$ quasars and AGNs faint with respect to their hosts. This sample provides an accurate link between low and high redshift AGN luminosity functions and does not suffer from the usual incompleteness of optical samples

¹Department of Astronomy, The Ohio State University, 140 W. 18th Ave., Columbus, OH 43210
[email:rjassef@astronomy.ohio-state.edu]

²Harvard-Smithsonian Center for Astrophysics, 60 Garden St., Cambridge, MA 02138

³W. M. Keck Postdoctoral Fellow at the Harvard-Smithsonian Center for Astrophysics

⁴School of Physics, Monash University, Clayton 3800, Victoria, Australia

⁵Peyton Hall, Princeton University, Princeton, NJ 08540

⁶Department of Astronomy, Bryant Space Science Center, University of Florida, Gainesville, FL 32611

⁷Department of Physics, Durham University, Durham DH1 3LE, UK

⁸KPNO/NOAO, 950 N. Cherry Ave., P.O. Box 26732, Tucson, AZ 85726

⁹CEA-Saclay, Service d'Astrophysique, Orme des Merisiers, Bat.709, 91191 Gif-sur-Yvette, FRANCE

¹⁰Center for Astrophysics and Space Sciences University of California, San Diego 9500 Gilman Drive La Jolla, California, 92093-0424

¹¹Jet Propulsion Laboratory, California Institute of Technology, 4800 Oak Grove Drive, Mail Stop 169-506, Pasadena, CA 91109

at $z \sim 3$. We use a set of low resolution SED templates for AGNs and galaxies presented in a previous paper by Assef et al. (2010) to model the selection function of these sources and apply host and reddening corrections. We find that the space density of the brightest quasars strongly decreases from $z = 3$ to $z = 0$, while the space density of faint quasars is at least flat, and possibly increasing, over the same redshift range. At $z > 3$ we observe a decrease in the space density of quasars of all brightnesses. We model the luminosity function by a double power-law and find that its evolution cannot be described by either pure luminosity or pure density evolution, but must be a combination of both. We used the bright end slope determined by Croom et al. (2004, 2QZ) as a prior to fit the data in order to minimize the effects of our small survey area. The bright-end power-law index of our best-fit model remains consistent with the prior, while the best-fit faint-end index is consistent with the low redshift measurements based on the 2QZ and 2SLAQ (Croom et al. 2009) surveys. Our best-fit model generally agrees with the number of bright quasars predicted by other LFs at all redshifts. If we construct the QSO luminosity function using only the IRAC-selected AGNs, we find that the biases inherent to this selection method significantly modify the behavior of the characteristic density $\phi_*(z)$ only for $z < 1$ and have no significant impact upon the characteristic magnitude $M_{*,J}(z)$.

Subject headings: galaxies: active — galaxies: distances and redshifts — galaxies: luminosity function, mass function — quasars: general

1. Introduction

Galaxies with active galactic nuclei (AGN) are among the brightest objects in the universe. Their light is thought to come from material accreting onto a super massive black hole (SMBH) that resides in the center of their host galaxies, so characterizing the AGN population and its evolution across cosmic time is a direct constraint on the formation and evolution of SMBHs. Recent theoretical studies (e.g., Hopkins et al. 2005; Di Matteo et al. 2005; Hopkins et al. 2006; Croton et al. 2006; Bower et al. 2006) have suggested AGN activity may play an integral role in the evolution of galaxies, so understanding AGN evolution may also constrain the paradigm of galaxy evolution. The simplest way to characterize these objects is by studying their spectral properties, their luminosity function, and how it evolves with redshift.

What we observe from an AGN depends on its luminosity relative to its host and the degree to which it is obscured by dust (e.g., Antonucci 1993). Broad line AGN are relatively

unobscured and divided into quasars and Type I Seyferts depending on the luminosity of the AGN. For the bright quasars it is far more difficult to observe the host galaxy than in the fainter Seyferts. Unification models posit that the narrow line Type II Seyferts are the same physical objects viewed from a direction along which the nucleus is obscured by dust. Absorption by dust reprocesses the shorter wavelength radiation from the accretion disc into mid/far-IR continuum radiation. Hard radiation escaping in other directions produces the narrow, high ionization lines characteristic of these objects. If the absorbing column becomes too thick, the nucleus can only be seen either in hard X-rays or radio with all other radiation reprocessed into the infrared.

AGN are relatively rare objects compared to galaxies and stars. Combined with their broad range of spectral properties, it is difficult to select large uniform samples across the broad redshift ranges needed to accurately characterize their evolution with cosmic time. Broad-band photometric redshifts for AGNs are not nearly as accurate as those for galaxies (e.g., Rowan-Robinson et al. 2008; Assef et al. 2010), so the samples selected from broad-band surveys must also be observed spectroscopically in order to confirm their nature and measure their redshifts. Medium- and narrow-band surveys can yield accurate photometric redshifts and circumvent the need for spectroscopic confirmation (Wolf et al. 2003; Salvato et al. 2009), but these surveys are uncommon. Most surveys used to derive QSO luminosity functions (QLFs) select targets based on optical broad-band colors and morphology. Such surveys work remarkably well at low and high redshifts but suffer from high incompleteness at $2.5 \lesssim z \lesssim 3.5$ where the optical colors of quasars are very similar to those of stars (Fan 1999). Several studies (e.g., Richards et al. 2006b; Brown et al. 2006; Croom et al. 2009) have shown that the density of bright quasars peaks at $z \sim 2$, so not being able to uniformly build the QLFs from redshifts well below to well above this peak is a limitation for understanding the evolution of nuclear activity with cosmic time. Surveys based on X-ray, mid-IR and radio do not have these limitations, but they are generally either too broad and shallow or narrow and deep to follow the full sweep of quasar evolution with cosmic time.

The AGN and Galaxy Evolution Survey (AGES; Kochanek et al. in prep.) is a redshift survey in the NOAO Deep Wide-Field Survey (NDWFS; Jannuzi & Dey 1999) Boötes field using the multi-object spectrograph Hectospec (Fabricant et al. 2005) at the MMT. Using the deep multi-wavelength observations of the NDWFS Boötes field to select targets, AGES obtained spectra for ~ 6000 AGN candidates and ~ 20000 galaxies with $I < 22.5$. In this paper, we present the rest-frame J -band luminosity function derived from the multi-wavelength photometric observations and the AGES spectroscopic observations of 1838 AGNs in the NDWFS Boötes field selected based on their Spitzer IRAC (Fazio et al. 2004) mid-IR colors, their MIPS (Rieke et al. 2004) $24\mu\text{m}$ fluxes, their X-ray counts in the XBoötes survey

(Murray et al. 2005), and their optical morphologies. These observations allow us to accurately study the evolution of the QLF from $z = 0$ to $z = 5.6$. In a companion paper (Assef et al. 2010, Paper I) we present a set of empirical SED templates that range from 0.03 to $30\mu\text{m}$ for galaxies and AGNs. We use these templates to model the AGES AGN selection function, to calculate absolute magnitudes and to correct for contamination from the host galaxy and extinction. In Dai et al. (2009), we present the mid-IR LFs of galaxies in the NDWFS Boötes field, while Cool et al. (in prep.) presents the optical LF of galaxies and Rujopakarn et al. (2010) presents their $24\mu\text{m}$ LF.

During the course of this paper we will interchangeably use the terms AGN and QSO to refer to all objects with active nuclei, regardless of inclination and luminosity. The technical differences between a QSO and a non-QSO AGN is a matter of contention in the current literature, but our sample spans a luminosity range large enough to encompass both groups, rendering a differentiation meaningless for our current purposes. The paper is organized as follows: in §2 we describe the photometric and spectroscopic observations we use; in §3 we detail the AGES AGN selection criteria and study the completeness of the spectroscopic observations; and in §4 we construct the mid-IR and X-ray selected QSO luminosity function across the redshift range of our sample, study its evolution and compare our results to previous studies at low and high redshifts. Two appendices outline the mathematics of including X-ray selected sources in our LFs and expand on the comparison between our results and other estimates of quasar LFs. We use an $\Omega_M = 0.3$, $\Omega_\lambda = 0.7$ and $H_0 = 73$ ($\text{km s}^{-1} \text{Mpc}^{-1}$) cosmology throughout the paper.

2. Data

The data set we use is described extensively in Assef et al. (2008) and in Paper I. Here we give a short description of it and refer the reader to those works for details. Our data consists of the extensive multi-wavelength photometric and spectroscopic observations of the NOAO Deep Wide-Field Survey (NDWFS; Jannuzi & Dey 1999) Boötes field. The NDWFS survey observed this field in the B_W , R , I and K bands. To this photometry, we have added observations, from blue to red, in the X-rays from the XBoötes survey (Murray et al. 2005), in the FUV and NUV channels of GALEX (Martin et al. 2005; release GR5, Morrissey et al. 2007), in the z -band from the zBoötes survey (Cool 2007), in J and K_s from the Flamingos Extragalactic Survey (FLAMEX; Elston et al. 2006), in all four IRAC channels ([3.6], [4.5], [5.8] and [8.0]) from the Spitzer Deep Wide-Field Survey (SDWFS; Ashby et al. 2009), and from the $24\mu\text{m}$ channel of MIPS (Weedman et al. 2006). Throughout this paper we will keep the conventions of each survey. All magnitudes are in the Vega system except for the AB

magnitudes used by GALEX (FUV and NUV) and zBoötes (z -band).

The AGN and Galaxy Evolution Survey (AGES; Kochanek et al. in prep.) obtained optical spectra for approximately 26000 objects in the NDWFS Boötes field, and of these, about 6000 were targeted as AGN candidates. Objects were targeted based on a broad range of photometric criteria. In particular, AGNs are divided into many uniform (non-exclusive) samples, based on their X-ray counts, radio emission, $24\mu\text{m}$ MIPS fluxes and IRAC colors (for details see Paper I, Kochanek et al. in prep.). In this paper we focus on the IRAC, MIPS and X-ray selected samples, and in the next section we discuss the different criteria by which these objects were targeted. We limit our sample to the main survey area and we eliminate areas close to bright stars, leaving an effective survey area of 7.47 square degrees.

We model the SEDs of each object using the templates derived in Paper I. Note that the X-ray fluxes are not used in the SED fits. Unlike Paper I, we use photometry measured in $3''$ diameter apertures instead of $6''$ in order to match the photometry used by AGES for spectroscopic targeting. We also drop the requirement of a minimum number of bands with detections or upper bounds (8 in Paper I) in order to not bias our sample. Nonetheless, all objects in our catalog, as defined in the next section, have at least 6 bands of observed photometry and at least 1 upper limit, which is enough for a well constrained SED fit (see Paper I).

3. Sample Selection

AGES used several different criteria to target AGNs for spectroscopic observations. In this Section we discuss in detail the selection of the sample we use in §4 to construct luminosity functions. In general, the bulk of the objects we consider have been selected by their IRAC colors, but because this selection has some important biases at low and high redshift, we complement it with objects targeted as AGN by their X-ray counts and by their MIPS fluxes.

3.1. IRAC Colors AGN Selection

Stern et al. (2005, but also see Lacy et al. 2004) empirically defined a region in the IRAC color-color diagram that encompasses the locus of QSOs and minimizes contamination by normal galaxies, although at the expense of eliminating some active objects (see Gorjian et al. 2008, Donley et al. 2008, Paper I). Based on Spitzer observations of the NDWFS field, AGES targeted prospective AGNs for spectroscopy using a set of 5 IRAC criteria

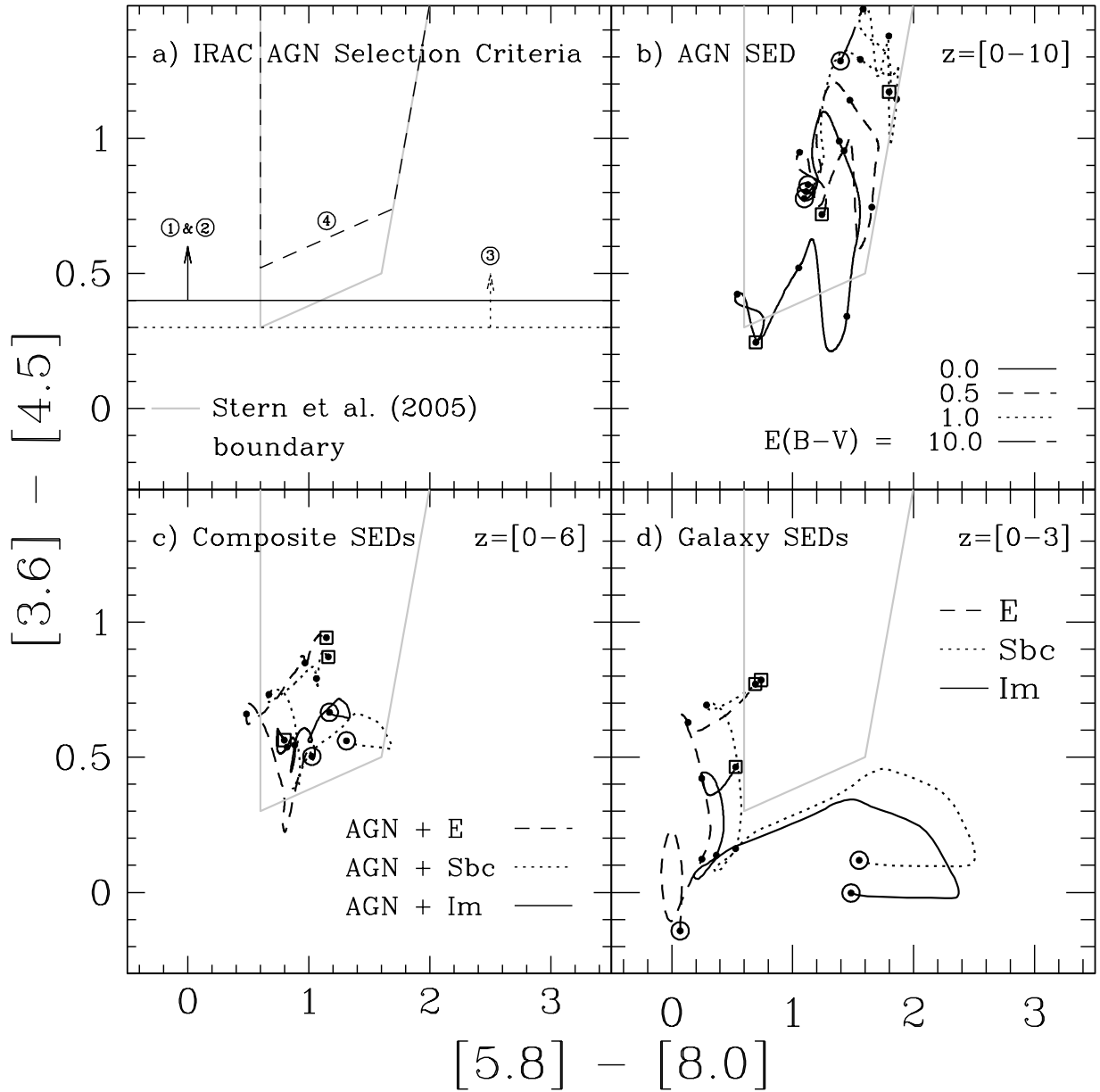


Fig. 1.— *a)* IRAC AGN selection criteria as detailed in §3 (we do not show criterion 5 as we do not consider it for building the AGN luminosity functions). *b)* IRAC color-color track of a pure AGN (i.e. no galaxy host) according to our templates. The tracks are shown for the redshift range $z = 0 - 10$ and four different levels of extinction. For a single track, the bulls-eye marks $z = 0$ and each successive black dot marks a redshift increase of 2. *c)* Same as *b)*, but for objects whose SED is, bolometrically, half AGN and half galaxy for each galaxy template separately, and only in the redshift range 0–6. For the AGN we have assumed no reddening. *d)* Same as *b)* and *c)* but for each galaxy template alone. Here the dots mark a redshift increase of 1 instead of 2, and we only show up to $z = 3$, as galaxies at higher redshifts are not relevant to our study.

that slightly differed from that of Stern et al. (2005) in order to increase or explore the completeness of the sample. These criteria are shown in Figure 1 and can be summarized as:

1. Optical point sources with observed magnitude $[3.6] \leq 18$ and color $[3.6] - [4.5] \geq 0.4$.
2. Optical point sources with observed magnitude $18 < [3.6] \leq 18.5$ and color $[3.6] - [4.5] \geq 0.4$, with the additional constraint of either $I - [3.6] \geq 3$ or $z - [3.6] \geq 3$ in order to limit stellar contamination.
3. Optical point sources with observed magnitude $[3.6] \leq 18$ and color $0.3 \leq [3.6] - [4.5] \leq 0.4$, again with the additional constraint of either $I - [3.6] \geq 3$ or $z - [3.6] \geq 3$ to limit stellar contamination.
4. Optically extended sources with observed magnitudes $I \leq 20$ and $[3.6] \leq 18.5$, and IRAC colors that put them inside the region shown in Figure 1. This is a conservative version of the region defined by Stern et al. (2005) in which the lower boundary is shifted 0.1 mag redwards.
5. Optically extended sources with observed magnitude $I \leq 22.5$ that otherwise satisfy the same constraints as in 4.

All colors are based on $3''$ aperture photometry (corrected for the PSF) and all total magnitudes correspond to **SExtractor** (Bertin & Arnouts 1996) “auto” magnitudes. Optical point sources are defined as objects that have a **SExtractor** stellarity index greater than 0.8 in any of the optical bands, namely B_W , R , I and z . The separation between optically extended and point sources should be quite reliable, as the 5σ depth of the depth of NDWFS is 25.5 magnitudes in I -band, 3 magnitudes fainter than the $I = 22.5$ limit of AGES.

The first criterion targets all point sources with a $[3.6]$ - $[4.5]$ color that would roughly put them inside the region defined by Stern et al. (2005) but disregards the information in the other two IRAC bands. The lower sensitivity of the two longer wavelength bands means that many more objects can be targeted based on the single $[3.6]$ - $[4.5]$ color than by requiring both colors. For the magnitudes we consider, we need not worry about the optically faint high redshift galaxies lying to the left of the Stern et al. (2005) criterion in Figure 1 (see Stern et al. 2005, Paper I). Criterion 2 targets fainter point sources with an extra constraint designed to eliminate normal stars as the color uncertainties increase, while criterion 3 attempts to target AGNs lost by the first two criteria due to emission lines passing through the $[3.6]$ channel at high redshifts, most notably $H\alpha$ at $z \simeq 4.5$ (see the discussion below, §4.3 of Paper I, and Richards et al. 2009).

Extended sources were targeted for spectroscopy if their IRAC colors put them inside the region defined by the modified Stern et al. (2005) boundaries of criteria 4 and 5. However, objects under criterion 5 were observed at a significantly lower priority than under criterion 4, and hence their spectroscopic completeness is very low. For this reason, we will only consider objects selected based on criteria 1–4 in the rest of the paper. This means that extended sources are limited to $I < 20$. Similarly, point sources with $I > 21.5$ were also observed at a lower priority than their brighter counterparts, resulting in significant incompleteness beyond this magnitude. To avoid dealing with the effects of large incompleteness, we adopt a faint magnitude limit of $I = 21.5$ for our point source AGN catalog. Note that, by doing so, we exclude the $z = 6.12$ quasar found by Stern et al. (2007) from our sample, as it has an I -band magnitude of ≈ 22 , but we keep all other $z > 5$ quasars found in the AGES sample (Cool et al. 2006).

Of the 1937 objects selected by these criteria, most correspond to galaxies with active nuclei, but there is some contamination by non-active sources. We have visually inspected all spectra and eliminated all objects that did not show broad emission lines unless they were classified as Type II AGNs by Moustakas et al. (2010) or were detected in X-rays with 4 or more counts (see §3.3), reducing our sample to 1459 “real” AGNs. We consider for this purpose as Type II AGNs all objects that have narrow line ratios above the limit of Kauffmann et al. (2003), which includes objects that can potentially be powered solely by star formation (see Kewley et al. 2001). Note that the Type II classification of Moustakas et al. (2010) requires that $H\alpha$ is contained in the wavelength range of the spectrum, effectively limiting this classification to $z < 0.4$. Of the 478 IRAC-selected objects we have dropped, only 114 (24%) are located inside the original Stern et al. (2005) selection region, confirming that the majority of these objects are contaminants due to the more relaxed selection criteria of AGES compared to Stern et al. (2005). The sources inside the Stern et al. (2005) diagram are likely a combination of contaminants due to photometric errors and “real” Type 2 AGN missed by the BPT classification (see discussion in §3.4 about the biases this may introduce in our results).

Figure 1 also shows the IRAC color tracks as a function of redshift for three classes of object: pure AGNs, objects with 50% AGN and 50% galaxy, where the percentages represent the contribution to the total “bolometric luminosity” (as defined in Paper I), and pure galaxies. Pure AGNs fall inside the region defined by Stern et al. (2005) at most redshifts regardless of reddening, with the exception of quasars with low reddening at $z \simeq 4.5$ and $z \gtrsim 7$, where $H\alpha$ and $H\beta$, respectively, are redshifted into the IRAC [3.6] channel making the colors overly blue (for a detailed discussion about this point see §4.3 of Paper I). Objects with combined AGN and galaxy components of equal luminosity (Fig. 1c) have colors that generally stay inside, but close to, the AGN selection boundary. Increasing the host galaxy

component will take these objects out of the selection region, especially when considering the smaller region used for optically extended AGNs. This is a bias against black holes accreting at low Eddington ratios, with the accretion limit up to which these selection criteria would target a given object being significantly dependent on the reddening of the central source and the overall SED of the source. For $z \lesssim 3$, the IRAC colors of galaxies are, by construction, strictly outside the AGN selection boundaries. At higher redshifts, galaxy colors overlap with those of active nuclei, but our sample is too shallow to include non-active galaxies at these distances.

The bias against quasars that are faint in relation to their hosts is further confirmed by Figure 2 (see also Hopkins et al. 2009). This Figure shows the IRAC colors of objects that do not meet the IRAC color criteria but have AGN signatures based on some other selection method. These correspond to objects that were either targeted by AGES as X-ray or $24\mu\text{m}$ sources (see §2 of Paper I), or that show narrow line ratios typical of type II AGN (at higher ratios than the maximum star formation line of Kewley et al. 2001) in the BPT diagram Baldwin et al. (1981) classifications of Moustakas et al. (2010). We limit the X-ray sources to objects with at least 4 counts in XBoötes because incompleteness is a significant problem below this limit (Kenter et al. 2005). The IRAC criteria selects almost all optically unresolved X-ray sources brighter than the $[3.6] \leq 18.5$ magnitude limit, but misses large numbers of $24\mu\text{m}$ MIPS sources and optically extended X-ray sources. The great majority of the MIPS sources correspond to star-forming galaxies at $z \sim 0.7$ that are compact enough to appear as optical point sources, but 46 of them show clear signs of AGN activity (see §3.2). Non-IRAC selected optically extended X-ray sources are likely real AGNs whose hosts dominate their IRAC colors (see Gorjian et al. 2008). This is primarily a problem at low redshifts, as high redshift sources are too bright to have SEDs dominated by their host galaxy.

As mentioned previously, unreddened AGNs at $z \sim 4.5$ have colors too blue to enter the sample. In particular, in the redshift range $4.10 \lesssim z \lesssim 4.95$, the IRAC-selected AGNs sample is highly incomplete, as it is too shallow to include reddened AGNs at these redshifts that would meet the selection criteria. The problem is similar to that of optical surveys at $2.5 \lesssim z \lesssim 3.5$ (Fan 1999), although here we are avoiding contamination by galaxies rather than stars. In fact, the MIPS selection criteria identified several quasars in this redshift range that were missed by the IRAC selection criteria because of their blue colors. In order to address the biases at low and high redshifts we have described, we include in our catalog all X-ray and MIPS selected AGNs with magnitudes $[3.6] < 18.5$ and $I < 21.5$ that are not flagged as such by their IRAC colors. In the following sections we describe these selection criteria in detail and how they complement our main IRAC-selected AGN sample.

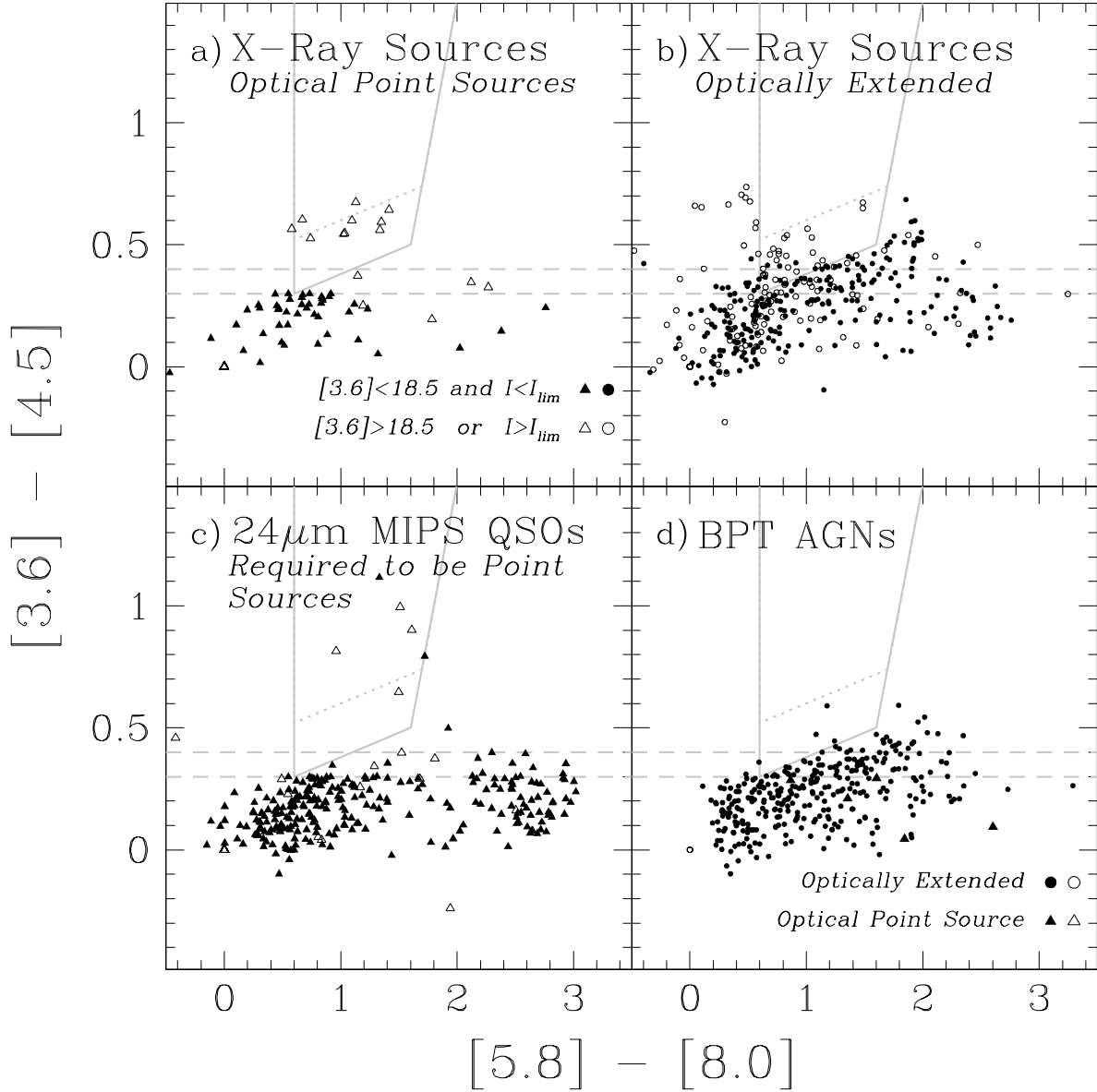


Fig. 2.— IRAC colors of spectroscopically observed objects with AGN signatures but *not* targeted as such based on their IRAC colors. We show objects targeted as X-ray sources, separated into optical point sources (*top left*) and optically extended objects (*top right*), as well as objects targeted as 24μm MIPS QSOs (*bottom left*). We also show objects classified as AGNs by their spectral line ratios in the BPT diagram (*bottom right*). In all panels, solid symbols show sources bright enough to make it into the IRAC selected samples, namely $[3.6] < 18.5$ and $I < I_{lim}$, while open symbols show sources fainter than either of these limits. Note that $I_{lim} = 21.5$ for optical point sources (*triangles*) and $I_{lim} = 20$ for the optically extended objects (*circles*).

3.2. MIPS Selection

The AGES MIPS quasar candidates are defined as optical point sources with $24\ \mu\text{m}$ MIPS fluxes $F_{24\mu\text{m}} > 0.3\ \text{mJy}$ and that have $3''$ I-band aperture magnitudes $I > 18 - 2.5 \log(F_{24\mu\text{m}}/\text{mJy})$. The limit on the I-band magnitude eliminates normal stars. The largest contaminants to this group are low redshift, strongly star-forming but optically unresolved galaxies, and intermediate redshift ($z \sim 0.7$) star-forming galaxies that are too distant to be resolved in the NDWFS survey. We also require that $I < 21.5$ and $[3.6] < 18.5$ in order to match the IRAC magnitude limits.

There are 264 objects targeted as AGN by their MIPS fluxes and optical morphology but not by their IRAC colors. As was done with the IRAC-selected objects in the previous section, we eliminate all objects that do not show broad emission lines in their spectra and that are not classified as Type II AGN by Moustakas et al. (2010). Under this criteria, we add 46 sources to our sample, of which 35 are at $z \leq 1$, 11 are at $z > 1$ and seven are at $z > 4$. We note that although the AGN selection efficiency is very low for this sub-sample (only 17% are real AGN), this is not the case for the full sample of MIPS targeted AGNs in the AGES survey, as there is a large overlap with the IRAC selection criteria. For example, if we take all objects in our sample targeted as AGN by the MIPS criteria, including the IRAC-selected ones, we find 1401 objects of which 968 (69%) are real AGNs.

3.3. X-Ray Selection

The X-ray AGN candidates in the AGES survey correspond to all optical sources matched with a probability of at least 25% to an X-ray source of 2 or more counts in the XBoötes survey according to the matching approach of Brand et al. (2006). The main contaminants are X-ray active stars along with a small number of very low redshift galaxies. To avoid stars, we eliminate all objects with redshifts below $z = 0.001$. We eliminate all objects detected with fewer than 4 counts, because below this flux the incompleteness of the XBoötes survey is high (Kenter et al. 2005). As done with the MIPS selection criteria, we require that $I < 21.5$ and $[3.6] < 18.5$ in order to match the IRAC magnitude limits. We assume all objects selected in this way correspond to real active nuclei. This adds 333 objects to our sample, of which 304 are optically extended and 29 are optical point sources. Of these objects, 330 have $z < 1$ and only 3, all optical point sources, have $z > 1$.

Table 1. AGN Sample

		All (1838)			IRAC (1459)			MIPS ^a (46)	X-RAY ^b (333)		
		Ext.	P.S.	Total	Ext.	P.S.	Total	P.S.	Ext.	P.S.	Total
All z	$I < 20$	344	585	929	40	557	597	18	304	10	314
	$I < 21.5$	344	1494	1838	40	1419	1459	46	304	29	333
$z < 1$	$I < 20$	344	225	569	40	203	243	13	304	9	313
	$I < 21.5$	344	408	752	40	347	387	35	304	26	330
$z > 1$	$I < 20$	0	360	360	0	354	354	5	0	1	1
	$I < 21.5$	0	1086	1086	0	1072	1072	11	0	3	3

Note. — The table shows the number of objects in our sample divided by selection criteria, redshift and optical extension (Ext. for optically extended sources and P.S. for point sources). The numbers in parenthesis correspond the total number of objects selected by each criteria. See §3 for details.

^aOnly objects not selected as IRAC AGNs.

^bOnly objects not selected as either IRAC or MIPS AGNs.

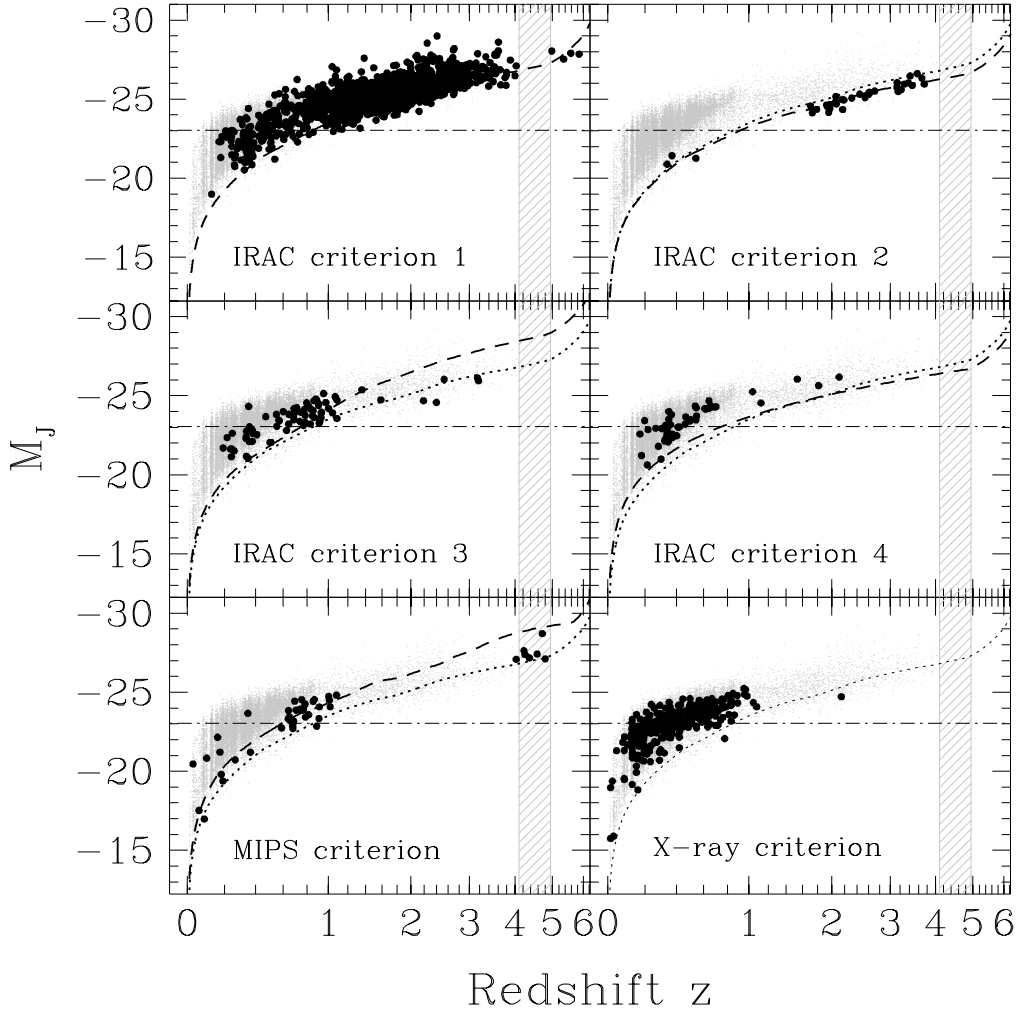


Fig. 3.— Magnitude-redshift relation of the sample used to derive the QSO luminosity function. Each panel shows one of the AGN targeting criteria of the AGES survey discussed in the text. Solid black circles show the AGNs targeted by each criteria while the gray dots show all other objects (except stars) in the survey, primarily normal galaxies. The dashed line in each panel shows the approximate J -band magnitude limit for the corresponding selection criterion, as extrapolated from the I and [3.6] band magnitude limits and the mean SED of each selection method. For the MIPS criterion we also include the $24\mu\text{m}$ magnitude limit of 0.3 mJy. We do not estimate this limit for the X-ray selected objects as the strongest constraints are in the X-rays, outside the range of our templates. For reference, in each panel the dotted line shows the J -band magnitude limit of the IRAC criterion 1. AGNs below the extrapolated magnitude limits are caused by a combination of photometric errors and host contamination below that of the average object of each class (see text for details). The vertical hashed regions shows the approximate redshift range on which our IRAC selected AGN sample contains no objects due to the contribution of the broad $\text{H}\alpha$ emission line to the [3.6] channel. The dot-dashed black horizontal line shows the characteristic Schechter function J -band luminosity $M_{*,J}$ for local galaxies from Cole et al. (2001).

3.4. The Full AGN Sample

Our final sample is described in detail in Table 1 and consists of 1494 optical point source and 344 optically extended AGNs. Note that in this Table, and in the remainder of this paper, the MIPS-selected sample refers to the sample of sources selected by their MIPS fluxes and optical extension (see §3.2) but not by their IRAC colors. Similarly, the X-ray selected sample refers to X-ray selected AGN not selected by either the MIPS or the IRAC criteria. Figure 3 shows the magnitude-redshift relations of these sources. Notice that there are no IRAC-selected sources at $4 \lesssim z \lesssim 5$, but that this redshift range is well populated by MIPS-selected QSOs, confirming the biases predicted by our SED templates. Note too that five objects targeted by the IRAC criterion 4 lie at $z > 1$. These objects were incorrectly classified as extended sources, and hence targeted by criteria 4 and 5 only. Upon visual inspection of the optical images, four objects seem to have slightly extended PSFs, although the nature of this is unclear, and the other has a very close companion, which likely affected the SExtractor stellarity index. We will consider them as optical point sources for the rest of the analysis, although they are such a small fraction of the objects that their treatment has little quantitative impact. Figure 3 also shows the approximate J -band magnitude limits for each selection criterion using the mean SED (normalized by bolometric luminosity) for each selection criterion. Objects seen below these model magnitude limits are caused by a combination of photometric errors and varying levels of host contamination compared to that of the mean SED. In particular, high redshift MIPS-selected objects are significantly fainter than the magnitude limit because the mean SED is dominated by the more numerous, host-dominated low-redshift sources. At low redshift, MIPS-selected objects not targeted by an IRAC criterion have hosts that are bright in relation to their AGN and hence the galaxy dominates their SED. At high redshift, however, they are bright quasars with very little host contamination to their SEDs that are missed by the IRAC criteria because of the $H\alpha$ broad emission line contribution to the [3.6] IRAC channel (see §3.1 for details). We account for all of these problems in the selection functions by using the individually observed SEDS to estimate them. Overall, our sample is still subject to one type of bias, related to the maximum reddening of AGNs of a given luminosity and host composition in our sample is a function of redshift, due primarily to the optical flux limit of AGES spectroscopy. The combination of IRAC, X-ray and MIPS targeting criteria is, by itself, not strongly affected by this bias, up to the point where the dust torus is self-obscuring in the mid-IR.

Notice that although we used the BPT diagram classification of Moustakas et al. (2010) to separate AGN from inactive galaxies for the IRAC and MIPS selection criteria, we do not include purely BPT-selected AGNs. The main reason is that this sample is limited to $z \leq 0.4$, and its inclusion would induce a systematic offset at this transition redshift in the QLF. Also note that the selection function of purely BPT-selected objects is more complex

than for the other samples, and it cannot be modeled with the tools we use here.

Given that our main reason for excluding purely BPT-selected AGNs is the limitation of $z \leq 0.4$, we need to understand if using the BPT diagram as a discriminator for contaminants in the IRAC- and MIPS-selected samples introduces a bias. To test for biases due to not being able to use the BPT method beyond $z = 0.4$, we took the IRAC and MIPS-selected AGNs solely confirmed as real AGNs by their BPT classification (i.e. no X-ray detection and no broad emission lines), fit their SEDs using the templates of Paper I, and modeled their selection as IRAC or MIPS AGN at higher redshifts. First, for the IRAC criteria, we find that the color of the mean SED of these objects is inside the selection regions only at $z \lesssim 0.6$ and $z \gtrsim 1.1$. Since we do not see non-active galaxies in our sample at $z > 0.8$ (see Paper I) due to the I-band limit of AGES, we can securely say that any bias introduced would only affect the redshift range $0.4 < z < 0.6$. In fact, 93 of the 114 IRAC-selected objects dropped in §3 but located inside the original Stern et al. (2005) selection diagram are at $z < 0.6$. For the MIPS criterion we find similar results. Of a total of 29 MIPS-selected AGN confirmed as real AGN solely due to their BPT classification, 15 (52%) would have met the selection criteria at $z > 0.4$ and only 2 (7%) would do so at $z > 0.6$. While it would be necessary to understand the luminosity function of these objects to assess the complete significance of this bias, these numbers suggest that the largest effect is in the $0.4 < z < 0.6$ range and of little importance at $z > 0.6$.

Our sample must be corrected for spectroscopic incompleteness in order to estimate the QSO luminosity function, as not all objects targeted for spectroscopy were observed, and redshifts could not be measured for all the observed objects. Let $P_S(m_I)$ be the probability that a spectrum of a given target was obtained, and $P_z(m_I)$ be the probability that a redshift was successfully measured from that spectrum, where both quantities are a function of the I -band observed magnitude of the source, m_I . We correct our sample by weighting each object by $[P_S(m_I)P_z(m_I)]^{-1}$. This weighting assumes that the targets were randomly observed and that unsuccessful redshift measurements are due solely to bad data. While the first assumption is generally true due to the design and observing strategy of the AGES survey, this is not completely clear for the second one. In particular, redshift measurements become easier for objects with stronger emission lines, which could in principle bias the objects with unsuccessful redshift measurements to have lower AGN luminosities. However, the QSO survey magnitude limit was $I = 22.5$, whereas we use a sample limited to a full magnitude brighter than this limit, so it should not be a major source of bias. Figure 4 shows P_S and P_z as a function of observed I -band magnitude, as well as the product of these two terms.

In the next section, we use this sample to study the QSO luminosity function and its

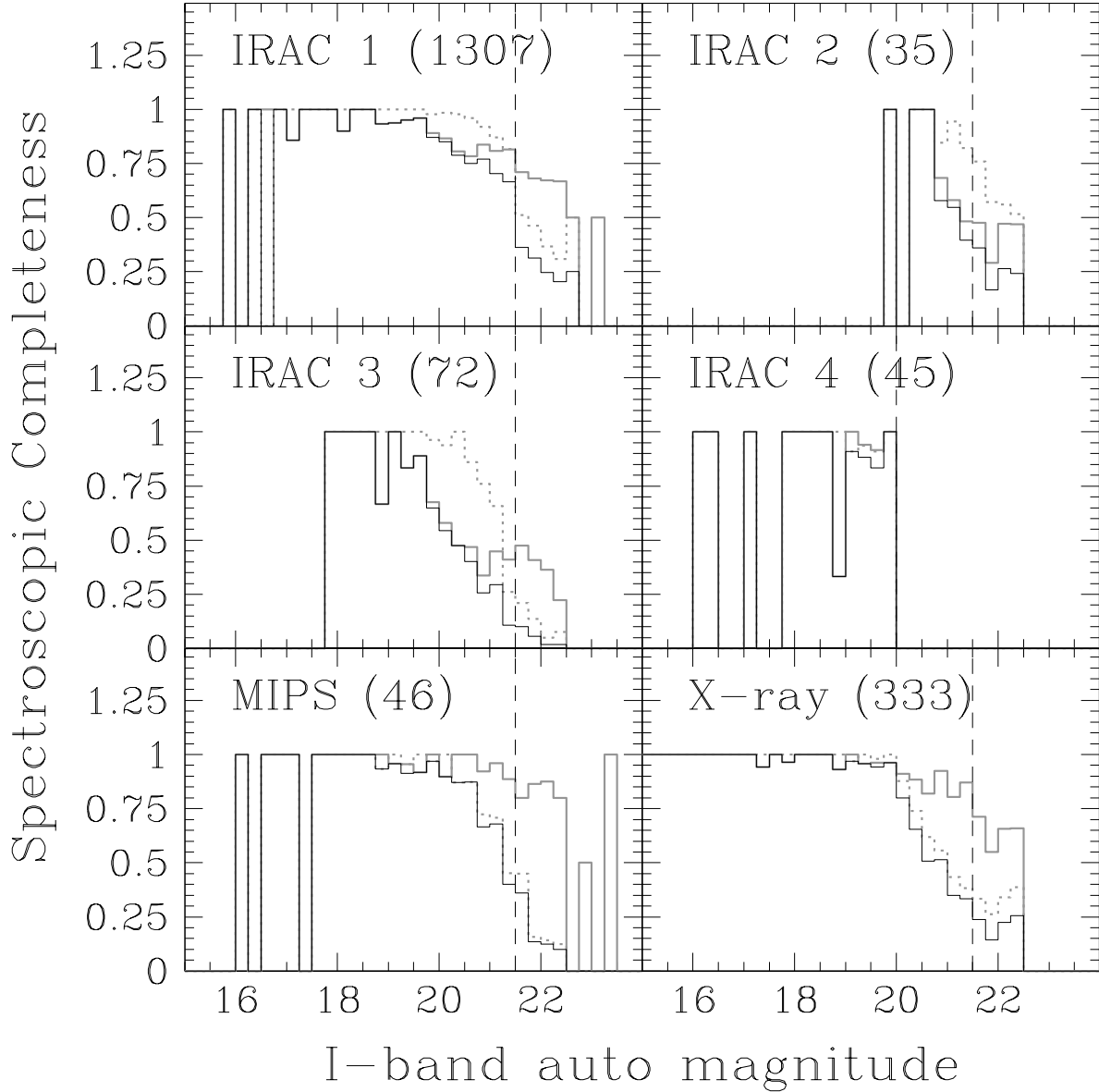


Fig. 4.— Spectroscopic completeness of our sample as a function of magnitude for each IRAC selection code discussed in §4.1. The solid gray line shows the fraction of objects as a function of I-band magnitude for which a spectrum was taken, while the dotted gray line shows the fraction of spectroscopically observed objects with a successful redshift measurement. The solid black line shows the product of the two, which is the inverse of the weight for an object of a given I -band magnitude when building the QLFs. The number in parenthesis is the number of objects in our sample from each category, and the vertical dashed line shows the magnitude limit to which we consider each selection criteria.

evolution with redshift. At $z < 0.75$ a significant number of objects are extended, and hence we use our full sample to determine the QLF. However, IRAC-targeted extended sources (criterion 4 of §3.1) are strictly bounded by $I_{\text{auto}} \leq 20$, and they represent 10% of the extended objects in the sample up to this magnitude limit. In order to have a complete sample, we limit our analysis at $z < 0.75$ only to objects brighter than this limit. For higher redshift bins, we use only optical point sources limited to $I_{\text{auto}} \leq 21.5$.

4. The mid-IR and X-ray Selected AGN Luminosity Function

In this Section we will study the luminosity function of AGNs in our sample. The combined data set described in §§2 and 3 is, by construction, well-suited to study the evolution of nuclear activity over a broad range of luminosities and redshift. The impact of each selection criteria upon the absolute magnitude limits as a function of redshift are illustrated in Figure 3. In this Section we will also discuss how our measurements compare to those determined by other groups.

4.1. Luminosity Function Determination

We constructed rest-frame J -band luminosity functions. We chose J -band because it is less affected by dust reddening than bluer bands and it overlaps with at least one of the near- to mid-IR bands available for our sample at every redshift. We use the Page & Carrera (2000) variant of the V/V_{max} method (Schmidt 1968) which constructs luminosity functions binned in absolute magnitude and redshift by weighting each object by the volume in which it could have been observed and still be part of our sample. We estimate the number of objects in a given magnitude and redshift bin as

$$\Phi(M_J, z) = \sum_i \left\{ W_i \int_{M_{J,\min}}^{M_{J,\max}} \int_{z_{\min}}^{z_{\max}} f_i(M'_J, z') \frac{dV}{dz'} dz' dM'_J \right\}^{-1} \quad (1)$$

where $M_{J,\min}$, $M_{J,\max}$, z_{\min} and z_{\max} are the edges of the magnitude and redshift bin respectively centered at M_J and z , V is the co-moving volume and W_i is the spectroscopic completeness of objects targeted by the same IRAC criteria as object i (as detailed in §3). The function $f_i(M'_J, z')$ is the probability that object i would have entered our sample if located at redshift z' with a J -band absolute magnitude M'_J . This function considers all the selection criteria for each object, and not just the one by which it was targeted. For each object, we estimate its best-fit SED from the templates presented in Paper I and then calculate the flux in each band assuming a redshift z' and a J -band magnitude M'_J to determine if the

object would have passed the IRAC or MIPS selection criteria. If it did, then $f_i(M'_J, z') = 1$. If not, but was detected by the X-ray criteria, $f_i(M'_J, z')$ takes the value of the X-ray detection probability, discussed in detail in Appendix A. Otherwise, we set $f_i(M'_J, z') = 0$. Note that, when calculating $f_i(M'_J, z')$, we correct the estimated [3.6] and I -band magnitudes by the difference between their $3''$ aperture and the auto magnitude values. Because many of the sources are at high redshift, we have added a prior based on the bright-end of the Las Campanas Redshift Survey (Lin et al. 1996) galaxy luminosity function to regularize the SED fits and avoid unphysically bright galaxy contributions to the SEDs (this is similar to the approach for photometric redshifts we used in Paper I). In practice, this means we maximize the probability

$$P \propto e^{-\chi^2/2} e^{-L_R/L_{*,R}}, \quad (2)$$

where the χ^2 term measures the difference between the data and the model SEDs only, and $L_{*,R}$ is taken from the results of Lin et al. (1996). Note that our main conclusions do not change if we eliminate this prior.

While the SED templates of Paper I do not explicitly include evolution corrections, evolution, which is largely just a shifting balance of star formation rates with redshift, is automatically included as evolution in the typical weights assigned to the templates with redshift. For example, passive evolution, to first order, is correctly modeled by reducing the average contribution of the early-type template relative to the later-type templates to the observed SEDs. Other evolutionary effects, like changes in the mean metallicity, are not considered in our SEDs templates, but their effects are also more subtle. We note, however, that in the higher redshift bins, our sample is composed primarily of Type 1 QSOs, and hence most evolutionary effects on the hosts would have small impacts upon the observed SEDs.

Figures 5 and 6 show the QSO luminosity functions for our complete sample. The data seems to be consistent with a double power-law shape, where the bright end rises towards faint magnitudes and the faint end is either constant or falling towards fainter magnitudes. The uncertain behavior at the faint-end is due to the small number of objects, and hence magnitude bins, at all redshifts and the large dispersion between them. Doubling the total number of magnitude bins at all redshifts does not modify the observed behaviour. We warn the reader, however, that some of the fainter magnitude bins may be unreliable due to the small amount of objects and the large space density corrections due to the survey limits. Also, the blended emission from the host galaxy affects the overall shape of the luminosity function. Unlike traditional optical QLFs, the host galaxy is a significant source of contamination in a J -band QLF, as rest frame J -band lies close to the $1.6\mu\text{m}$ stellar emission peak and the minimum of the AGN SED (see Figure 2 of Paper I).

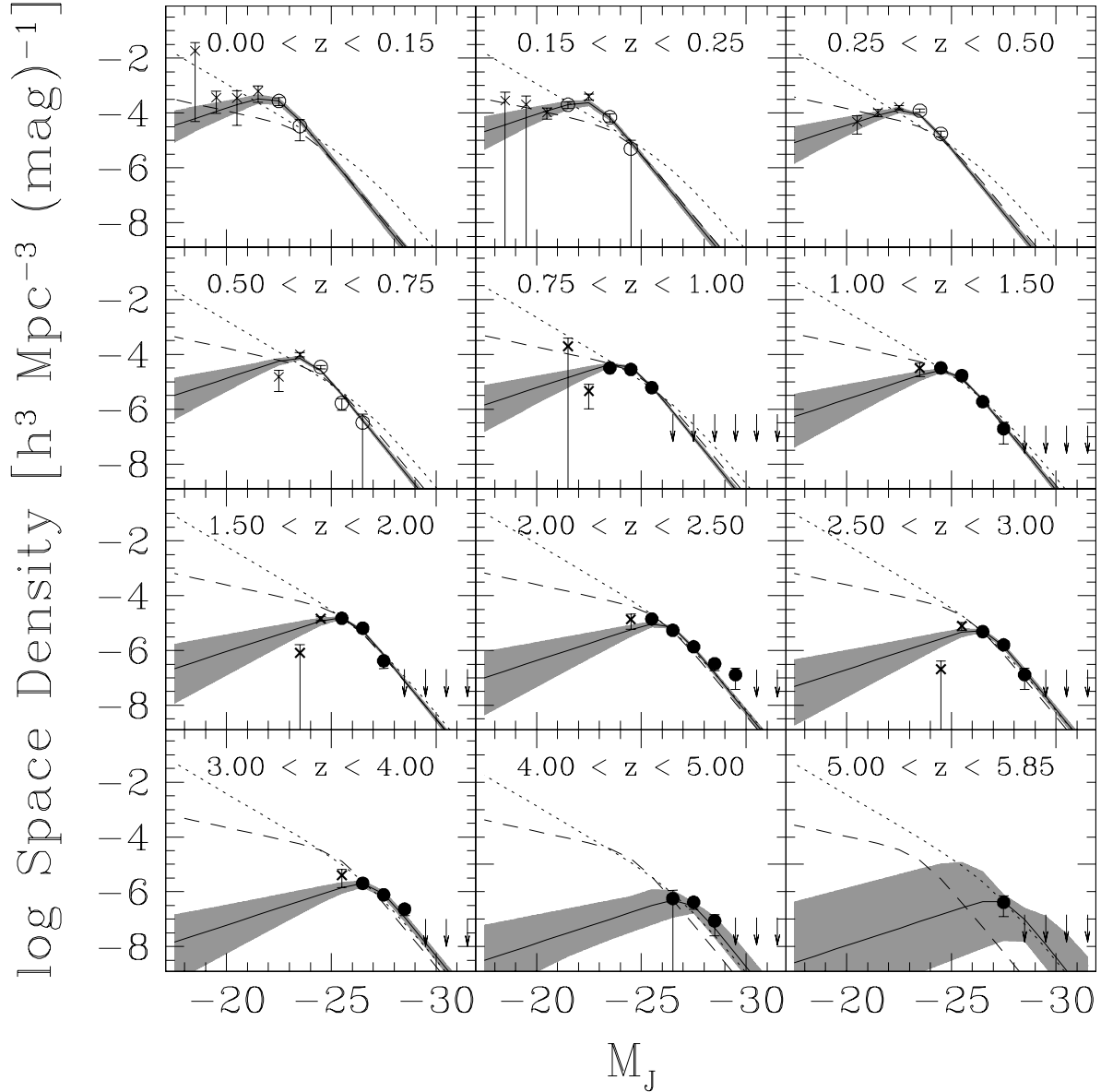


Fig. 5.— J -band luminosity function of our X-ray and mid-IR selected sample for several redshift bins. Here, the magnitudes have *not* been corrected for host contamination and reddening. At redshift $z < 0.75$, the QLF is constructed from a combination of optically extended and point sources with $I < 20$ (*open circles*), while for $z > 0.75$ it is constructed using only point sources with $I < 21.5$ (*solid circles*). The crosses show points that were not used in the fits, as described in the text. The best-fit luminosity and density evolution (LDE), pure luminosity evolution (PLE) and pure density evolution (PDE) models are shown by the solid, dashed and dotted line respectively, although only the LDE model is an acceptable fit to the data. The shaded region shows the 2σ ($\Delta\chi^2 \leq 4$) confidence region for the LDE fit.

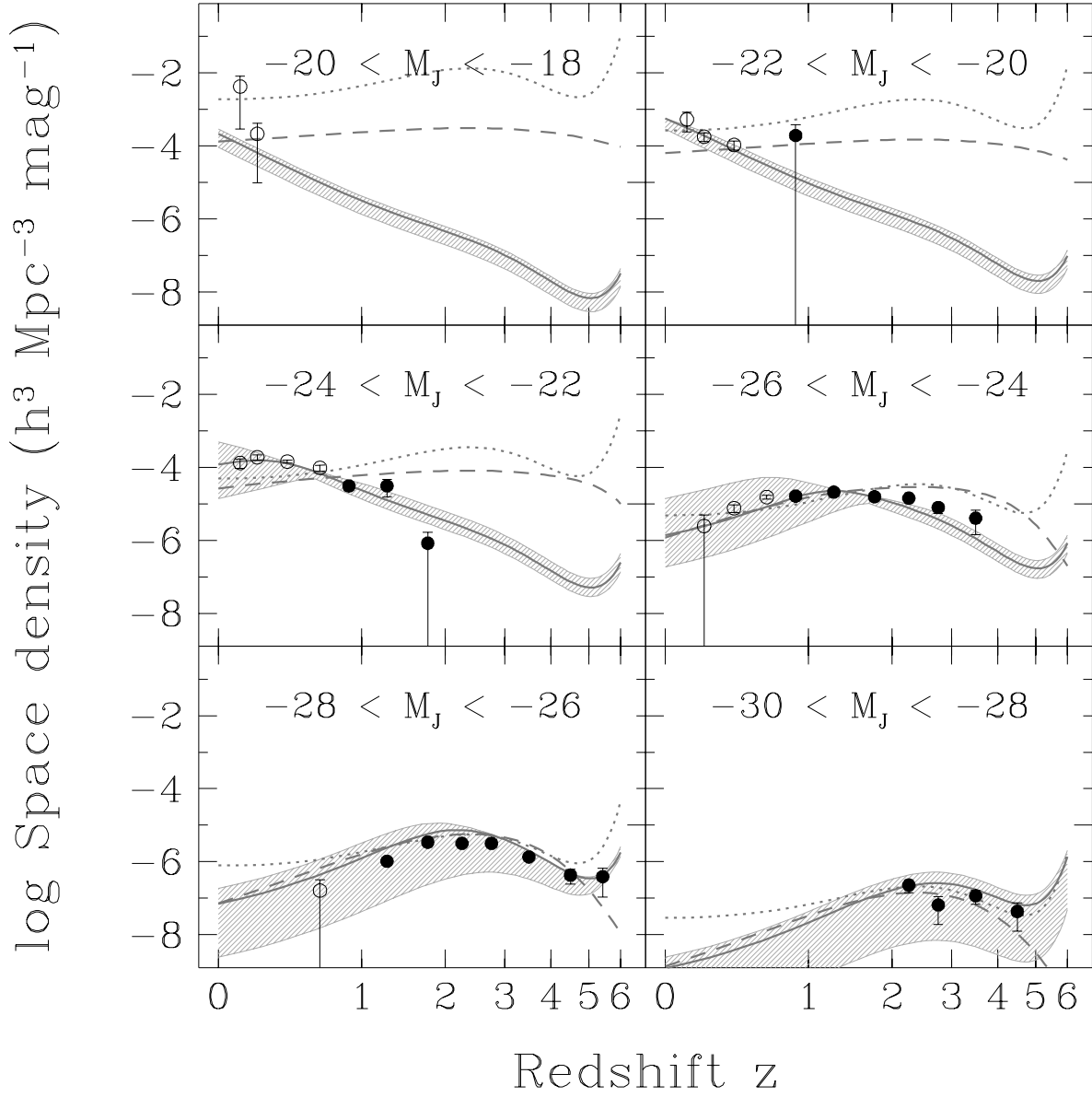


Fig. 6.— As in Figure 5, but showing the space density of quasars as a function of redshift for several absolute magnitude intervals. The models are drawn based on the median magnitude of the objects in each M_J bin. The hashed region shows the full range of space densities corresponding to each bin of our best-fit LDE model. The turn-over at $z > 5$ is unlikely real.

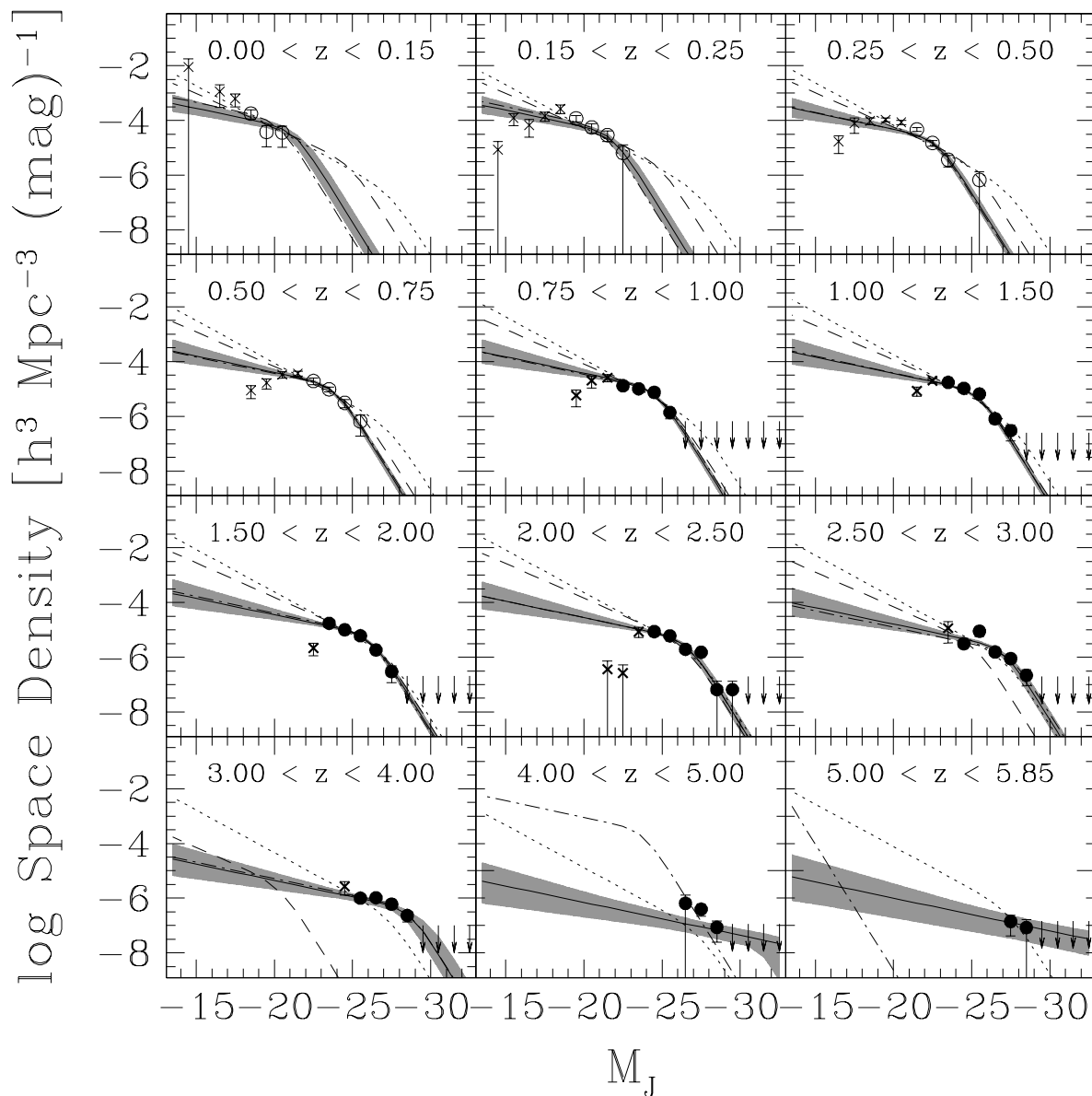


Fig. 7.— Same as in Figure 5 after removing host contamination. The dot-dashed line shows the best-fit allowing for an extra order in the $M_{*,J}(z)$ polynomial ($n = 5$).

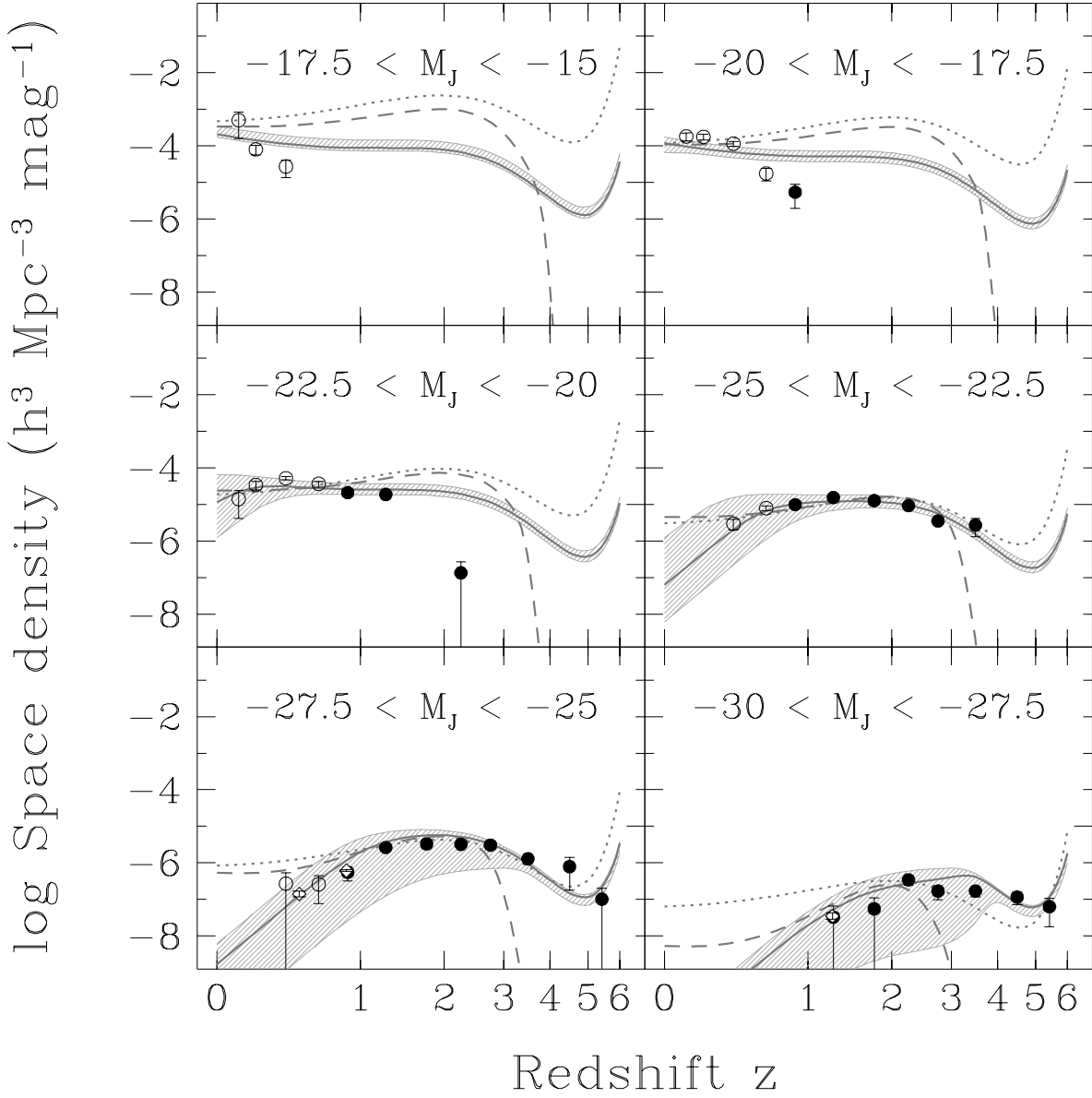


Fig. 8.— Same as in Figure 6 after removing host contamination. The white rhombi in the two brightest magnitude bins show the lowest redshift space densities derived by Richards et al. (2006b) using the SDSS survey. The agreement is very good, as these points overlap with our measurements. Note that to convert M_J to the redshift 2 i -band used by Richards et al. (2006b) we have used our AGN template with a reddening of $E(B-V) = 0.05$, as discussed in §4. The upwards turn at $z > 5$ is likely an artifact created by the small number of objects in the highest redshift bins coupled with the functional form of the model.

We use our SED templates to subtract the host contribution and recalculate the QLF. We also correct the absolute magnitude for the estimated reddening of the AGN, although this is not a major correction at this wavelength — the median reddening of $E(B-V) = 0.06$ changes the $1.2\mu\text{m}$ flux by only 5%. Figures 7 and 8 show the resulting host-corrected QLFs. Since this is a much more physically meaningful representation of the QSO luminosity function, we will refer to it as the “true” QLF for the rest of the paper. The luminosity functions seems to be again best described by a double power-law. Due to the small survey volume at low redshifts, the high luminosity power-law is not present at $z < 0.25$ because such objects are so rare. Unlike the QLF found prior to removing the host contamination, the faint end (without including the faintest magnitude bins), seems to be increasing to fainter magnitudes, although with a much shallower slope than that of bright quasars. Most redshift bins also show a significant turnover at the faintest magnitudes. We do not believe this to be real, but is again caused by small numbers of objects and large space density corrections. Uncertainties in the host subtraction may also play a role, although it is hard to quantify.

Just as we can use our template SED models to remove the host, we can also estimate the “bolometric” luminosity function of QSOs. In this case, the bolometric luminosity corresponds to the integrated light of the unreddened best-fit AGN template to the observed SED of each object over the wavelength range between 1216\AA and $30\mu\text{m}$. The QSO bolometric luminosity functions are shown for several redshift and magnitude bins in Figures 10 and 11. The bolometric and host corrected QLFs are very similar since there is a simple relation between L_{AGN} and M_J for each individual source.

4.2. Parametric fits to the QLF

We model the QSO luminosity function (QLF) as a broken power-law,

$$\Phi(L_J, z) dL_J = \Phi_*(z) \left\{ \left[\frac{L_J}{L_{*,J}(z)} \right]^{-\alpha} + \left[\frac{L_J}{L_{*,J}(z)} \right]^{-\beta} \right\}^{-1} \frac{dL_J}{L_{*,J}(z)}, \quad (3)$$

where α and β are free parameters and we allow for both luminosity and density evolution. This functional form is also used by, for example, Croom et al. (2004) and Richards et al. (2005) to study the low redshift QSO luminosity function. While in principle the shape of the QLF can be a function of redshift, we hold α and β fixed, as our sample lacks the high dynamic range in luminosity at all redshifts that would be needed to explore this.

Note that our overall field size is small, so we have few high luminosity quasars and our ability to constrain the bright-end slope of the QLF is limited. This is not the case for β ,

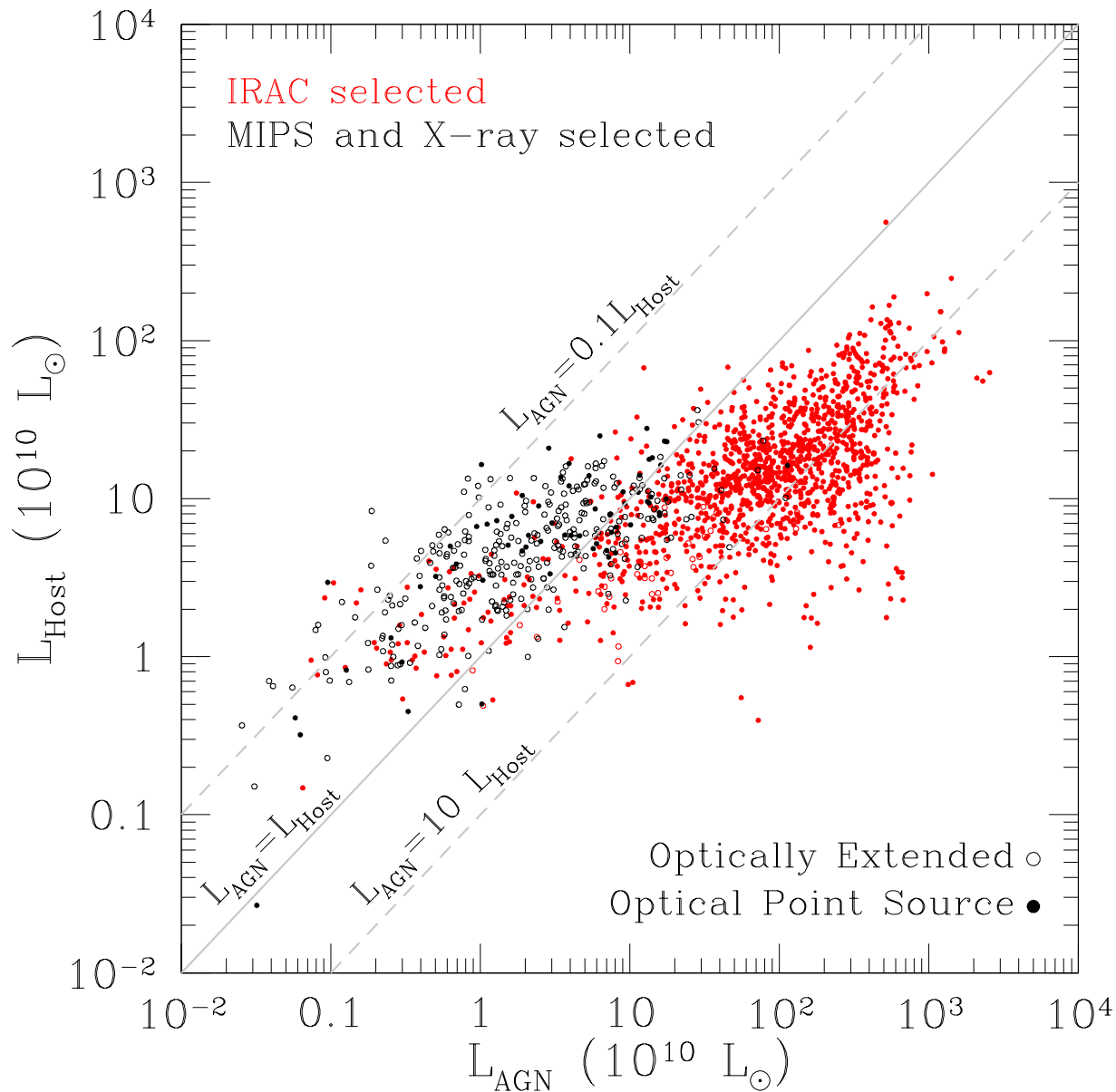


Fig. 9.— “Bolometric” luminosity of the best-fit AGN component against that of the best-fit host component for all objects in our sample. Solid circles show optical point sources while open circles show optically extended objects. IRAC selected AGN are shown in red while MIPS and X-ray selected ones are shown in black.

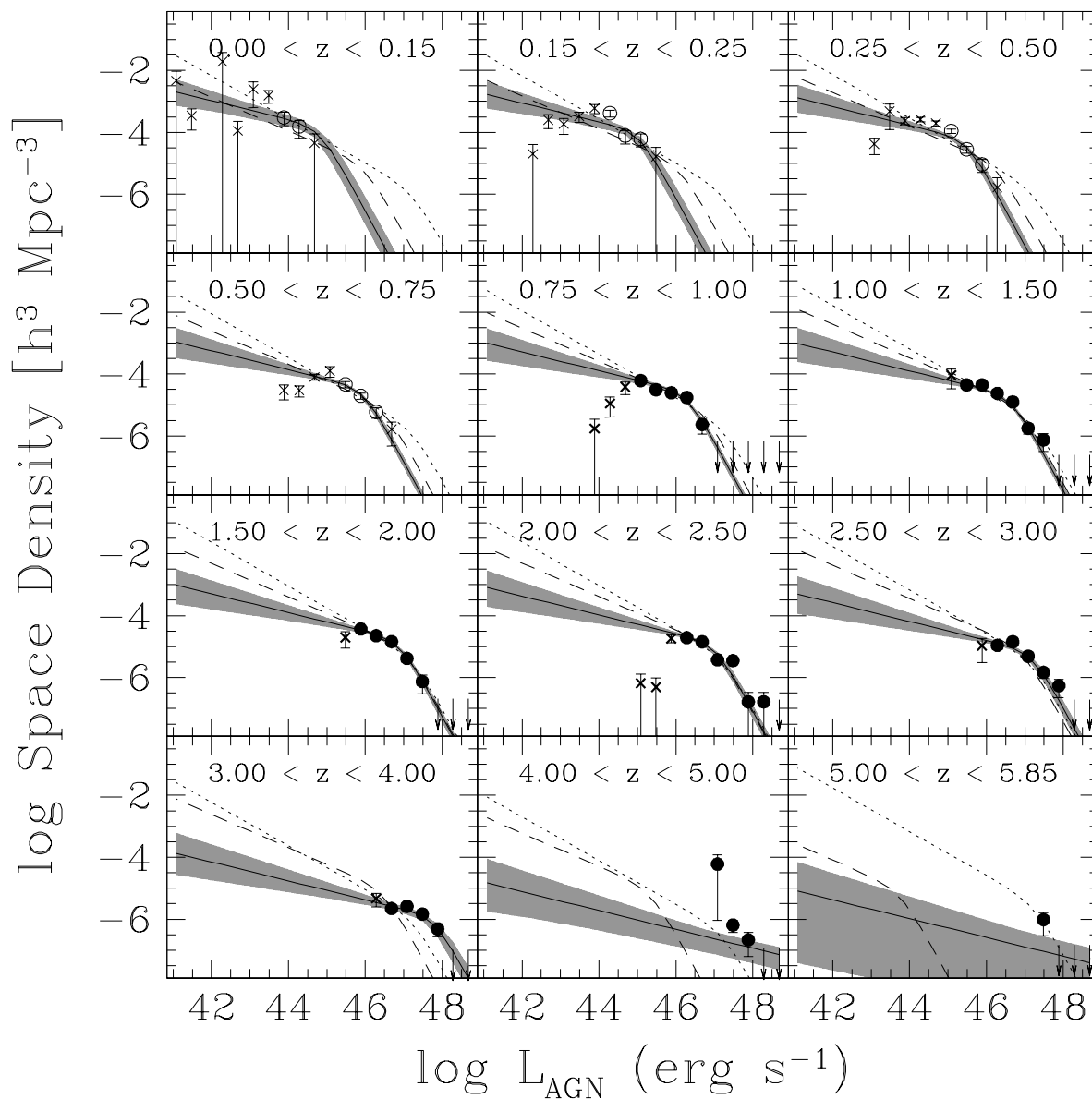


Fig. 10.— Bolometric QSO luminosity function. Lines and points have the same definition as in Figure 5.

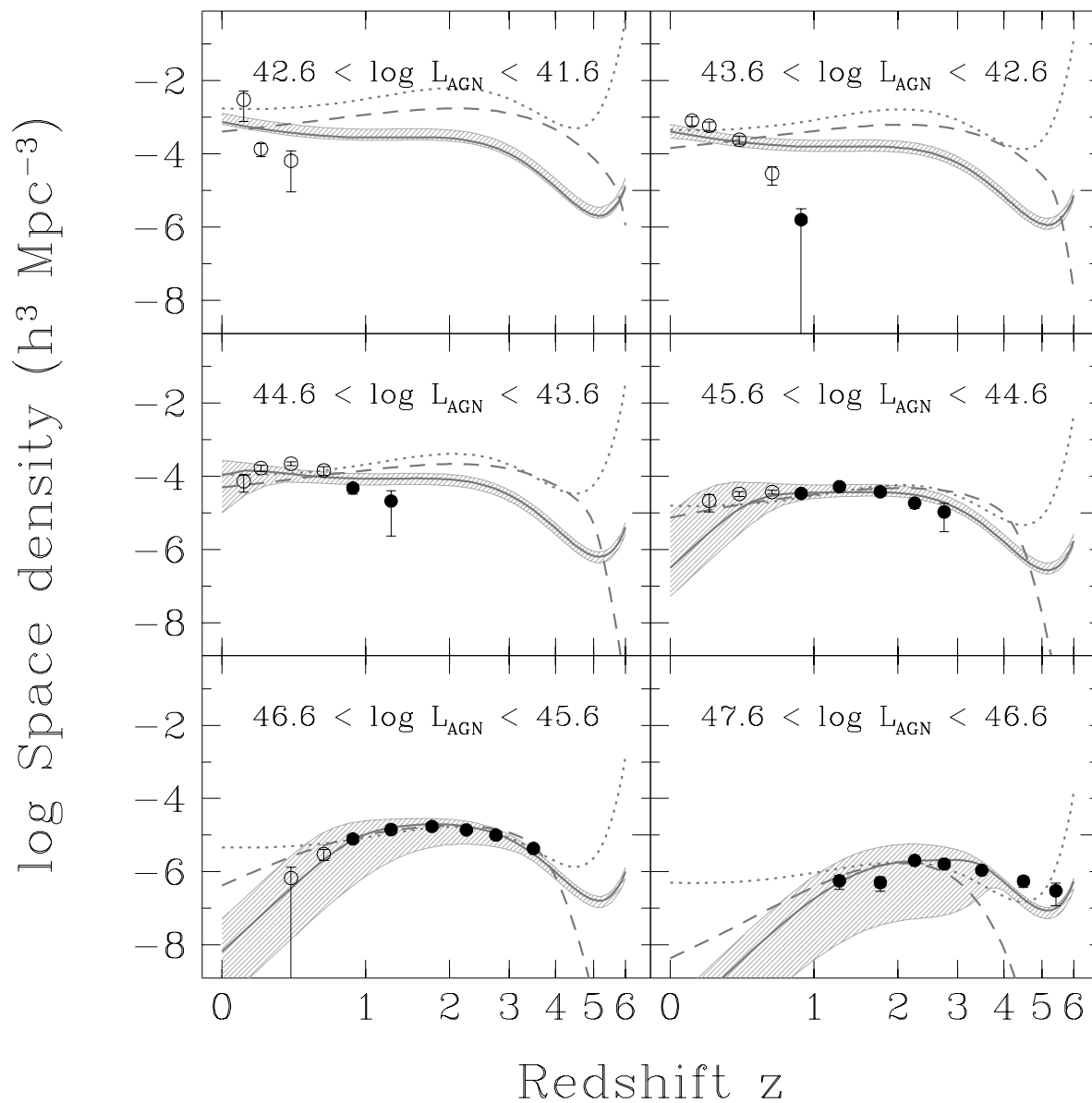


Fig. 11.— Redshift evolution of the bolometric QSO luminosity function for several magnitude bins. Lines and points have the same definition as in Figure 6. As for Figures 6 and 8, the upwards turn at $z > 5$ is unlikely real.

as the depth of the survey allows for a secure determination of this parameter. This is in contrast to wide area shallow surveys, like 2QZ (Croom et al. 2004) and SDSS (York et al. 2000), that cover large areas to shallow depths and can securely constrain α but not β . We included a Gaussian prior on the bright-end slope $\alpha = -3.31 \pm 0.05$ based on the results of the 2QZ survey. This estimate for α comes from their fits using a redshift polynomial (see eqn.[5] below) for the evolution of M_* rather than the model using the exponential evolution as a function of look-back time (see §4.3).

We model the break magnitude $M_{*,J}$ and its evolution by an n^{th} degree Lagrange interpolation polynomial

$$M_{*,J}(z) = \sum_{i=1}^n M_{*,J}(z_i) \prod_{k=1, k \neq i}^n \frac{(z - z_k)}{(z_i - z_k)}, \quad (4)$$

where the $M_{*,J}(z_i)$ are free parameters. This parametrization is equivalent to the commonly used polynomial form (e.g., Croom et al. 2004; Richards et al. 2005; Brown et al. 2006)

$$M_*(z) = M_*(0) - 2.5 \sum_{j=1}^{n-1} k_j z^j, \quad (5)$$

but the $M_{*,J}(z_i)$ parameters are more physically meaningful and have weaker covariances than the k_j parameters, as they simply represent the value of $M_{*,J}$ at different redshifts. Similarly, we model the density evolution by

$$\log[\Phi_*(z)] = \sum_{i=1}^n \log[\Phi_*(z_i)] \prod_{k=1, k \neq i}^n \frac{(z - z_k)}{(z_i - z_k)}, \quad (6)$$

where all $\Phi_*(z_i)$ are free parameters. Note that, because our sample covers a large spread in redshift around the peak at $z \sim 2$, we must use $n \geq 4$ so that the evolution of the QLF parameters can be asymmetric around the peak. In practice, we take $n = 4$ for modeling $M_{*,J}(z)$ and $n = 5$ for modeling $\log[\Phi_*(z)]$. For $M_{*,J}(z)$, $z_k = (0.5, 1, 2, 4)$, while for $\log[\phi_*(z)]$, $z_k = (0.25, 0.5, 1, 2, 4)$. The choice of the z_k affects only the covariances of parameters — the underlying polynomial is independent of the choice and depends only on the polynomial order.

We perform the fits for the three different cases of (1) luminosity and density evolution (LDE, all 11 parameters are allowed to vary), pure luminosity evolution (PLE, $\Phi_*(z)$ is replaced by a single parameter Φ_*) and pure density evolution (PDE, $M_{*,J}(z)$ is replaced by a single parameter $M_{*,J}$). In the PLE and PDE models there are 7 and 8 free parameters respectively. In all cases we use the Levenberg – Marquardt χ^2 minimization algorithm including the prior on the value of α .

To fit the observed J -band QLF we drop faint end magnitude bins that contain 2 or fewer objects. We also drop bins at all magnitudes that have V/V_{\max} corrections to their space densities greater than a factor of 2, for $z < 4$. Faint bins with so few objects and large space density corrections are easily dominated by systematic errors in the SED fits or in the V/V_{\max} method. We note that for the host corrected J -band luminosity function at $z < 4$ there is only one magnitude bin with 2 or less objects and a V/V_{\max} correction factor smaller than 2. This is the faintest bin of the $0.15 < z < 0.25$ redshift range, which is clearly well below any nearby data point. At $z > 4$, all magnitude bins are used in the fits, as there are too few objects to do otherwise. We note, however, that all the $z > 4$ bins have small correction factors ($< 50\%$ corrections), except for the faintest bin with $4 < z < 5$ of the host corrected J -band and bolometric luminosity QLF. Removing this data point, however, changes the best-fit parameters by much less than 1σ , and hence does not play a fundamental role in determining the best-fit functional form to the observed QLFs.

The fits are summarized in Tables 2, 3 and 4, respectively, for the three versions of the QLF we introduced in the previous section: the J -band QLF uncorrected for host contamination (Figs. 5 and 6), the J -band QLF corrected for host contamination (Figs. 7 and 8), and the AGN bolometric luminosity QLF (Figs. 10 and 11). The fits are shown in each of the respective Figures, along with the 2σ ($\Delta\chi^2 \leq 4$) confidence region of the LDE fit. The relatively small confidence region at the highest redshift bins in spite of the few data points is driven by a combination of the small error bars of many of the data points in combination with the stiffness of the model constrained by the lower redshift bins. Note that we do not count the bright-end upper limits in accounting for the number of degrees of freedom. In all cases the LDE fit gives a much better description of the data. In particular, for the host corrected J -band QLF, the χ^2_{ν} is larger by a factor of 1.9 for the PDE model and by a factor of 2.1 for the PLE model. This strongly argues that the nature of the QSO LF evolution is a combination of changes in characteristic magnitude of the AGNs and changes in the total number of these objects as a function of cosmic time, both effects with similar strengths. This is compatible with the recent results of Croom et al. (2009), who observed a similar behavior in a combined sample of SDSS and 2SLAQ QSOs (see §4.3).

As discussed before, our sample lacks the high dynamic range to study the redshift evolution of the power-law slopes, and hence we have assumed them to be redshift independent in the LDE, PLE and PDE models we fit. There is evidence that the bright-end slope may evolve with redshift (see, e.g., Richards et al. 2006b; Hopkins et al. 2007; Croom et al. 2009), and hence a fixed value of α may bias the rest of the LF parameters. While we cannot fit for an evolutionary form of α , we can assess the effects its evolution may have on the rest of the parameters. For this we modify the LDE model by including a redshift-dependent $\alpha(z)$

Table 2. J-band QSO Luminosity Function Parametric Fits

Parameter	LDE	PLE	PDE
χ^2	49	155	180
χ^2_ν	2.053	5.536	6.657
α	-3.35 ± 0.05	-3.30 ± 0.05	-3.30 ± 0.05
β	-0.37 ± 0.27	-1.42 ± 0.18	-2.13 ± 0.08
$M_{*,J}$	-26.71 ± 0.37
$M_{*,J}(z = 0.5)$	-23.51 ± 0.13	-24.52 ± 0.18	...
$M_{*,J}(z = 1.0)$	-24.64 ± 0.10	-25.16 ± 0.18	...
$M_{*,J}(z = 2.0)$	-26.10 ± 0.09	-25.81 ± 0.18	...
$M_{*,J}(z = 4.0)$	-27.08 ± 0.22	-25.10 ± 0.21	...
$\log \phi_*^a$...	-4.53 ± 0.11	...
$\log \phi_*(z = 0.25)$	-3.41 ± 0.11	...	-5.92 ± 0.28
$\log \phi_*(z = 0.50)$	-3.73 ± 0.08	...	-5.83 ± 0.26
$\log \phi_*(z = 1.00)$	-4.17 ± 0.06	...	-5.58 ± 0.24
$\log \phi_*(z = 2.00)$	-4.65 ± 0.05	...	-5.14 ± 0.24
$\log \phi_*(z = 4.00)$	-5.77 ± 0.12	...	-5.68 ± 0.27
$M_{*,J}(0)$	-22.05	-23.65	...
k_1	1.31	0.80	...
k_2	-0.30	-0.20	...
k_3	0.02	0.01	...

Note. — The best-fit parameters of our luminosity and density evolution (LDE), pure luminosity evolution (PLE) and pure density evolution (PDE) model fits to the QLF. For each parameter we quote the formal 1σ error-bars from the Levenberg – Marquardt fitting algorithm. For an easier comparison with other results in the literature, we also show the values of the parameters of the more commonly used functional form for the evolution of M_* shown in equation (5). We show no error-bars for this values as correlations between them can be highly significant.

^a $\text{h}^3 \text{Mpc}^{-3} \text{mag}^{-1}$

Table 3. Host Corrected J-band QSO Luminosity Function Parametric Fits

Parameter	LDE	PLE	PDE	LDE- $\alpha(z)$	LDE _{STY}	LDE _{STY} ^{β}
χ^2	62	154	137	61
χ^2_ν	1.630	3.677	3.341	1.605
α_0	-3.17 ± 0.05
α	-3.30 ± 0.05	-3.31 ± 0.05	-3.31 ± 0.05	...	-3.30	-3.30
β	-1.30 ± 0.08	-1.63 ± 0.06	-1.77 ± 0.05	-1.26 ± 0.09	-1.15 ± 0.05	-1.30
$M_{*,J}$	-27.51 ± 0.34
$M_{*,J}(z = 0.5)$	-23.32 ± 0.21	-25.12 ± 0.24	...	-23.15 ± 0.25	-22.68 ± 0.13	-23.29 ± 0.09
$M_{*,J}(z = 1.0)$	-25.00 ± 0.17	-25.81 ± 0.25	...	-24.98 ± 0.18	-24.50 ± 0.10	-25.04 ± 0.09
$M_{*,J}(z = 2.0)$	-26.44 ± 0.18	-26.81 ± 0.25	...	-26.26 ± 0.19	-26.49 ± 0.10	-26.66 ± 0.07
$M_{*,J}(z = 4.0)$	-30.86 ± 1.15	-14.23 ± 2.03	...	-31.18 ± 1.78	-28.49 ± 0.14	-30.14 ± 0.21
$\log \phi_*^a$...	-5.48 ± 0.12
$\log \phi_*(z = 0.25)$	-4.46 ± 0.12	...	-6.52 ± 0.21	-4.34 ± 0.13	-4.46	-4.46
$\log \phi_*(z = 0.50)$	-4.72 ± 0.09	...	-6.41 ± 0.18	-4.65 ± 0.10	-4.67 ± 0.02	-4.65 ± 0.02
$\log \phi_*(z = 1.00)$	-4.99 ± 0.08	...	-6.16 ± 0.16	-4.97 ± 0.08	-4.96 ± 0.03	-4.89 ± 0.04
$\log \phi_*(z = 2.00)$	-5.22 ± 0.08	...	-5.89 ± 0.16	-5.16 ± 0.09	-5.33 ± 0.04	-5.19 ± 0.04
$\log \phi_*(z = 4.00)$	-7.06 ± 0.27	...	-6.98 ± 0.20	-7.02 ± 0.36	-6.75 ± 0.07	-6.88 ± 0.08
$M_{*,J}(0)$	-20.57	-24.93	...	-19.97	-20.09	-20.54
k_1	2.72	-0.17	...	3.20	2.42	2.67
k_2	-1.12	0.77	...	-1.42	-0.75	-1.02
k_3	0.18	-0.25	...	0.23	0.09	0.15

Note. — The best fit parameters of each of our three models for the QLF with the formal 1σ error-bars from the Levenberg – Marquardt fitting algorithm. For an easier comparison with other results in literature, we also show the values of the parameters of the more commonly used functional form for the evolution of M_* shown in equation (5). We show no error-bars for this values as correlations between them can be highly significant. This Table also shows the parameters obtained by varying the prescription of the fitting algorithms to explore possible systematic errors in our results, as discussed in §4.2. Best fit parameters under the heading LDE- $\alpha(z)$ correspond to those obtained fitting the binned LF with the LDE model but assuming an α that evolves according to the results of Hopkins et al. (2007). Those under the headings LDE_{STY} and LDE_{STY} ^{β} were obtained with the STY method either fitting for β or fixing it to -1.3, respectively (see §4.2 for details).

^a $\text{h}^3 \text{Mpc}^{-3} \text{mag}^{-1}$

Table 4. Bolometric QSO Luminosity Function Parametric Fits

Parameter	LDE	PLE	PDE
χ^2	64	144	149
χ^2_ν	1.818	3.681	3.922
α	-3.31 ± 0.05	-3.30 ± 0.05	-3.30 ± 0.05
β	-1.30 ± 0.07	-1.54 ± 0.06	-1.70 ± 0.04
$\log L_*^a$	46.80 ± 0.11
$\log L_*(z = 0.5)$	45.24 ± 0.08	45.93 ± 0.10	...
$\log L_*(z = 1.0)$	45.97 ± 0.07	46.30 ± 0.08	...
$\log L_*(z = 2.0)$	46.51 ± 0.07	46.62 ± 0.09	...
$\log L_*(z = 4.0)$	48.25 ± 0.36	45.54 ± 0.16	...
$\log \phi_*^b$...	-5.01 ± 0.10	...
$\log \phi_*(z = 0.25)$	-4.02 ± 0.12	...	-5.84 ± 0.17
$\log \phi_*(z = 0.50)$	-4.31 ± 0.09	...	-5.79 ± 0.15
$\log \phi_*(z = 1.00)$	-4.61 ± 0.08	...	-5.58 ± 0.13
$\log \phi_*(z = 2.00)$	-4.80 ± 0.08	...	-5.28 ± 0.12
$\log \phi_*(z = 4.00)$	-6.67 ± 0.22	...	-6.23 ± 0.16

Note. — The best fit parameters of each of our three models for the bolometric QLF with the formal 1σ error-bars from the Levenberg – Marquardt fitting algorithm.

^a erg s^{-1}

^b $\text{h}^3 \text{Mpc}^{-3}$

that evolves according to the best-fit functional form of Hopkins et al. (2007), given by

$$\alpha(z) = \frac{2\alpha_0}{[(1+z)/(1+z_{\text{ref}})]^{k_{\alpha,1}} + [(1+z)/(1+z_{\text{ref}})]^{k_{\alpha,2}}}, \quad (7)$$

where $z_{\text{ref}} \equiv 2$. We keep $k_{\alpha,1}$ and $k_{\alpha,2}$ fixed to their best-fit values in Hopkins et al. (2007, Table 3) and we let α_0 vary, subject to a Gaussian prior based on the value in Hopkins et al. (2007). We refer to this model as LDE- $\alpha(z)$. Its best fit parameters are listed in Table 3 and all are within $1\text{-}\sigma$ of those obtained assuming a redshift independent bright-end slope, with a very slight improvement in χ^2_ν of 0.025. This shows that the assumption of a non-evolving bright-end slope is not a significant source of bias in our results.

The best-fit LDE model, as shown in Figure 8, implies that the number of faint AGNs ($M_J > -20$) is roughly constant in the redshift range from 3 to 0. The behavior of the data-points at $M_J > -20$ is consistent at the lowest redshift bins but seems to deviate for $z > 0.5$, suggesting a decrease in the number of AGNs. We cannot tell if this behavior is real or not, as these points correspond to the faintest magnitude bins at a given redshift range which we have argued before are the most likely to be affected by systematic errors. The brighter objects ($M_J < -20$) have a roughly constant density down to a certain redshift after which their space density decreases rapidly to lower redshifts. The redshift of this inflection points seems to increase for brighter magnitudes, showing a very clear trend of downsizing of AGN activity. The data are generally consistent with this picture, however the constraints are weaker. The drop in space density of bright quasars with diminishing redshift is consistent with the data, although the large error bars limit the significance. These large error bars are a direct consequence of the small area of the Boötes field. However, if we simply superpose the space densities measured from the shallower but 1000 times larger area SDSS survey (Richards et al. 2006b) on our estimates for the two brightest magnitude bins, we find excellent agreement, confirming the strong evolution of bright quasars. To convert between the different bands, we used our AGN SED template with $E(B - V) = 0.05$ (see §4.3). We do not use these SDSS data in fitting the LDE model shown in Figure 8.

Note that for the host-corrected QLF, the best-fits for all three models have negative values of both α and β , unlike for the uncorrected QLF. This is in much better agreement with what has been found by several other studies. The fact that this change is induced by the host contamination removal suggests that lower luminosity AGNs tend to have lower $L_{\text{AGN}}/L_{\text{Host}}$ ratios, or in other words, that they tend to be in relatively brighter host galaxies. By removing the host component, the J-band absolute magnitude of the faint objects become fainter, depopulating the region around the magnitude break and populating the faint end of the QLF, while the brightest part of the bright end is relatively unaffected. Although there is no *a priori* reason to expect a correlation between L_{AGN} and $L_{\text{AGN}}/L_{\text{Host}}$, we see exactly

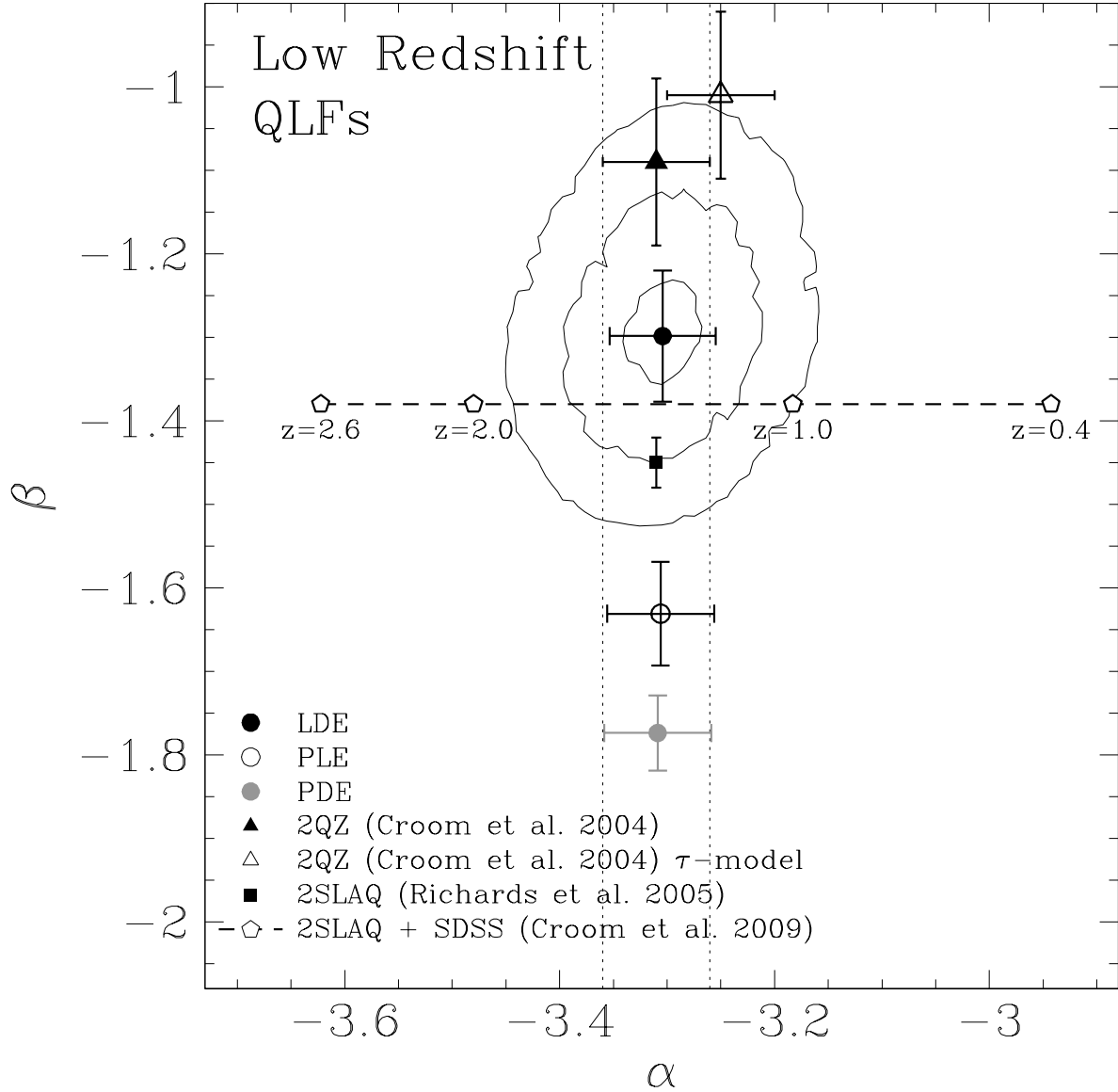


Fig. 12.— Best-fit values of the parameters α and β to our data (see eqn. [3]) for the LDE (black solid circle), PLE (open circle) and PDE (gray solid circle) models. Error-bars are the formal errors determined by the Levenberg – Marquardt minimization technique. Contours show regions of constant $\Delta\chi^2$ of 1, 4 and 9 (solid black line). The vertical dotted black lines show the 1σ interval of the prior used on the parameter α . For comparison, we show values of other studies determined by using low redshift samples (see §4.3 for details). In particular, we show the best-fit values determined by Croom et al. (2004) using the 2QZ survey observations, by Richards et al. (2005) using early data from the 2SLAQ survey and by Croom et al. (2009) using a combination of the finalized 2SLAQ survey data and the QSO SDSS sample of Richards et al. (2006b).

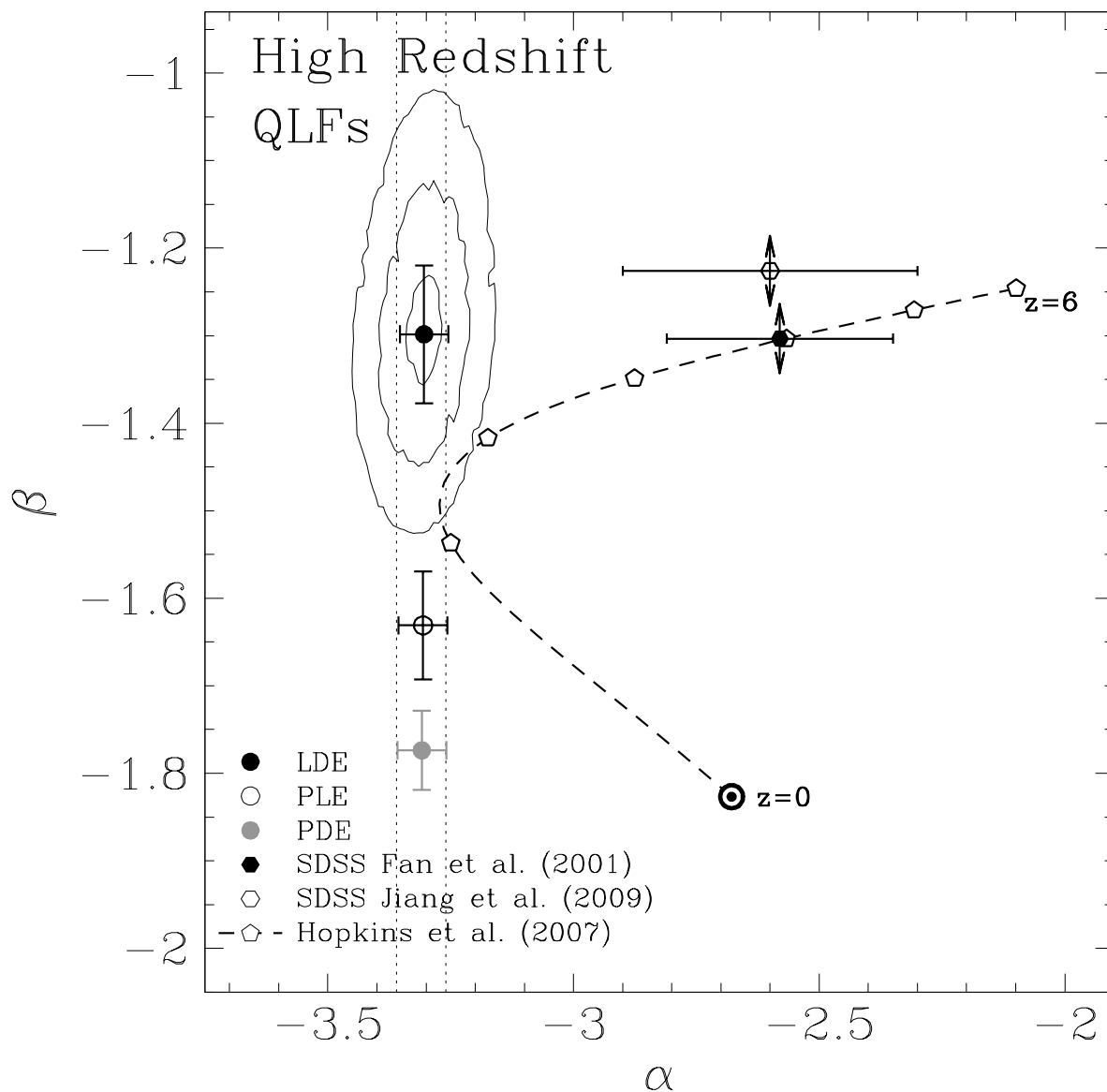


Fig. 13.— Same as Figure 12, but here we compare to parameters fitted to high redshift samples. In particular we show the best-fit α values of Fan et al. (2001) and Jiang et al. (2009) determined using a sample of high redshift QSOs from SDSS (see §4.3 for details). We also show the best-fit values of α and β determined by Hopkins et al. (2007) as a function of redshift. The target shows the values at $z = 0$ and then pentagons mark the different values at redshift intervals separated by $\Delta z = 1$ up to $z = 6$ (also see §4.3 for details).

this trend in Figure 9, which compares the “bolometric” luminosity of the host and AGN components of the best-fit SED. Note that the detailed distribution of the sources is subject to two biases. First, $L_{\text{AGN}}/L_{\text{Host}}$ must be large enough for the source to be recognized as an AGN, but small enough for the host luminosity to be measured from the SED fit, and second, we can detect high luminosity sources over larger volumes. However, neither of these should affect the general trend that the region of $L_{\text{AGN}}/L_{\text{Host}}$ occupied by sources is a strong function of L_{AGN} . It is worth noting that Hopkins et al. (2005b) predicts, based on simulations of galaxy mergers that include AGN feedback processes, that the faint-end of the AGN luminosity function is populated by massive black holes accreting at sub-Eddington rates rather than by small black holes radiating at the Eddington limit, much in line with what we find here.

Figures 12 and 13 show our estimates for α and β , and their uncertainties, as compared to other estimates (see §4.3 for details). The error-bars in our measurements correspond to the formal errors calculated from the Levenberg – Marquardt fit, while the contours show regions of constant $\Delta\chi^2$ (1, 4 and 9 respectively). Figure 14 shows the evolution of $M_{*,J}(z)$ and $\phi_*(z)$ and their 2σ ($\Delta\chi^2 \leq 4$) uncertainties. We note that for $z < 3$, the evolution of $M_{*,J}$ and $\log[\Phi_*(z)]$ is roughly linear with $\log(1+z)$, suggesting that, at least in this range, $\log(1+z)$ would be a more natural parameter to describe their evolution. At redshifts $z \geq 3$ the evolution of both parameters show significant departures from linearity in $\log(1+z)$, but this is not necessarily well constrained. It is clear from Figure 7 that the highest redshift bins only weakly constrain these parameters, as all the data points are fainter than $M_{*,J}$.

We experimented with changes in the order of the interpolation polynomials from $n = 4$ for the evolution of $M_{*,J}(z)$ and $n = 5$ for $\log[\Phi_*(z)]$. Reversing the number of parameters ($n = 5$ for $M_{*,J}(z)$ and $n = 4$ for $\log[\Phi_*(z)]$) gives qualitatively similar fits, albeit with a slightly worse χ^2_ν for the LDE model. Decreasing the number of parameters results in a worse fit to the data as well. For example, $n = 5$ for $\log[\Phi_*(z)]$ and $n = 3$ for $M_{*,J}(z)$ results in an increase of χ^2_ν of approximately 0.2, while $n = 4$ for both parameters produces an increase of approximately 0.3. While $n = 4$ for $M_{*,J}(z)$ and $n = 5$ for $\log[\Phi_*(z)]$ do not fit the QLF with $\chi^2_\nu = 1$, we choose to not add more degrees of freedom. Our LFs are somewhat noisy and higher degrees of freedom will fit the noise. For example, in the host corrected luminosity function, using $n = 5$ for both parameters improves the χ^2_ν by ≈ 0.24 , better describing the lower redshift bins at the cost of being unable to reproduce the highest redshift measurements by a significant margin (see Figure 7).

Miyaji et al. (2001) has argued that the method of Page & Carrera (2000) may bias the constructed luminosity function with respect to the true underlying shape due to binning effects. To test for this biases we refit the LDE model using the method of Sandage et al.

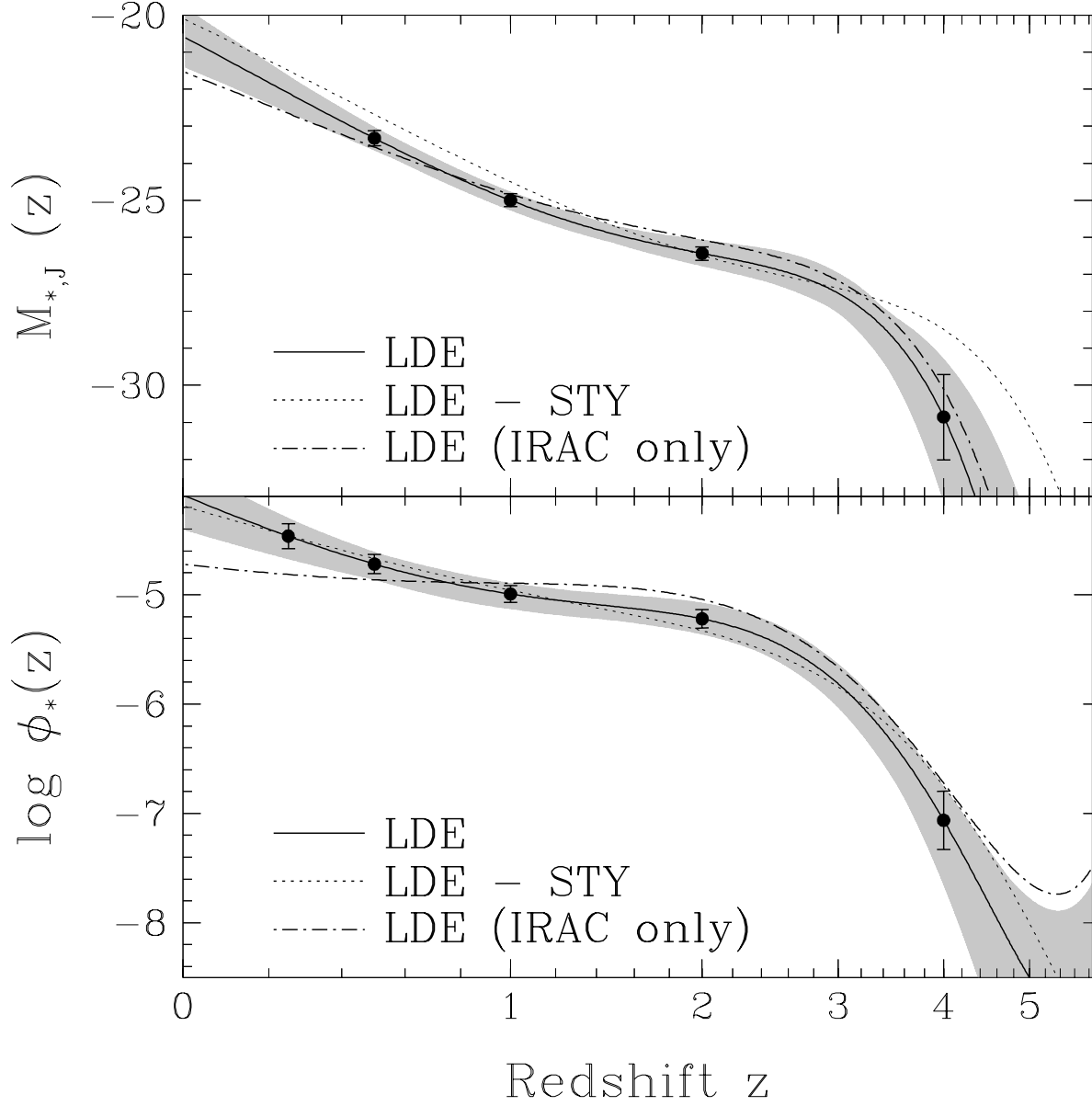


Fig. 14.— (*Top panel*) The best-fit evolution of $M_{*,J}$ from our LDE model for the full QSO sample and that obtained from our LDE model (*solid line*) for the IRAC selected sample only (*dot-dashed line*). We also show evolution obtained using the STY estimator to fit the LF (*dotted line*). The gray shaded area shows the $2\text{-}\sigma$ ($\Delta\chi^2 \leq 4$) range spread of the evolution from the LDE fit. The points show the respective values of the best-fit $M_{*,J}(z_k)$ parameters (see eqn. [4]) for this model and their respective error-bars from the Levenberg – Marquardt fitting routine. (*Bottom Panel*) The best-fit evolution of ϕ_* . The solid, dot-dashed and dotted lines, points and the gray shaded region have the same meaning as in the above panel.

(1979, STY) in the formulation of Efstathiou et al. (1988). The STY method fits the model to the unbinned data, removing the biases discussed by Miyaji et al. (2001). We note, however, that it is not possible to include the upper bounds on the bright-end of the LF in this formulation. For this experiment we held $\alpha = -3.30$ fixed to the best-fit value of the LDE model to the binned data. We also fixed the lowest redshift characteristic density parameter to set a density scale, as the STY method cannot determine the absolute normalization of the space density. We find that all of the best fit parameters are within the 2σ range of the values found for the binned LF. Moreover, the shape of the evolution of $M_*(z)$ and $\phi_*(z)$ is relatively unchanged from those obtained using the binned LFs (see Fig. 14). The faint-end slope, β , is flatter than for the binned LF by 2σ . While most of the $M_{*,k}$ parameters are fainter than for the binned LF, this is due to the larger value of β and its covariance with $M_*(z)$. If we repeat the fits holding $\beta = -1.30$ to match our previous fits, we find $M_{*,k}$ parameters in very good agreement with those obtained by fitting the binned LF (see Table 3). Given that the changes in the parameters are only modest, fitting the parametric models to the binned luminosity functions is not an important source of systematic errors and does not bias our conclusions.

4.3. Comparison with Other Measurements

In the previous sections, we constructed the QSO luminosity functions of mid-IR and X-ray selected AGNs in the NDWFS Boötes field from $0 \lesssim z \lesssim 6$ using several different functional forms to describe the shape and evolution of the QLF. We settled on a standard best-fit LDE model. In this section we make a broad comparison of our results to those in the literature for optical, mid-IR and X-ray selected AGNs. Detailed comparisons with other works can be found in Appendix B. A significant complication to this comparison is the very different wavelengths of our measurements compared to other surveys. Wavelength corrections are particularly important when comparing the predicted densities of quasars, as a uniform magnitude limit must be assumed. We use the unreddened AGN template presented in Paper I to convert between wavelengths and make uniform comparisons between surveys. Some of the QLFs we compare to, however, are measured at rest-frame UV, and hence the conversion from our J -band measurements is very dependent on the shape of the SED. As discussed in Paper I, the optical slope of our template is bluer than typical AGN SEDs, as it tries to match the bluest quasars in the sample rather than the average object. To account for this, we also present some results using our AGN template with $E(B - V) = 0.05$, which better matches the UV part of the Richards et al. (2006a) mean Type-I quasar SED. Table 5 shows the rest frame color $X - J$ used for each case discussed in this Section, where X is the corresponding rest-frame band used by each study, for both values of the reddening. For

reference, as discussed in Paper I, we have assumed a reddening that follows an SMC-like extinction curve for $\lambda < 3300\text{\AA}$ and a Galactic extinction curve at other wavelengths, with $R_V = 3.1$ for both regimes.

Figure 15 shows the space density of bright AGNs ($M_J < -25$) predicted by our best-fit LDE model as a function of redshift, along with the predictions of the best-fit functional form of other studies in the literature. In particular, we show the results of Croom et al. (2004, 2QZ survey), Croom et al. (2009, 2SLAQ and SDSS), Fan et al. (2001, SDSS), Jiang et al. (2009, SDSS), Brown et al. (2006, AGES – MIPS selected $8.0\mu\text{m}$ LF), Wolf et al. (2003, COMBO–17) and Hopkins et al. (2007). A detailed description of each study (bands, target selection and result comparison) is given in Appendix B. Color transformations based upon our unreddened AGN SED are appropriate for QLFs constructed in optical and mid-IR rest-frame (2QZ, $8\mu\text{m}$ AGES and Hopkins et al. 2007), while the reddened AGN template color conversion is more appropriate for UV rest-frame QLFs (COMBO-17, 2SLAQ and SDSS). In general, Figure 15 shows the agreement is relatively good with most other studies, although discrepancies are present. In most cases the discrepancies can be attributed to the small sample sizes of some of the studies (Wolf et al. 2003; Brown et al. 2006; Fan et al. 2001) or of some of the redshift ranges in our sample (again, see Appendix B for a detailed comparison). Note the general agreement at the redshift of the peak of our distribution ($z \sim 2$) with all other studies that encompass this redshift. The largest disagreements comes from the SDSS-based study of Richards et al. (2006b) at $z \sim 2$, however since their sample is a sub-sample of that used by Croom et al. (2009), which shows remarkable agreement, the discrepancies are unlikely to be important.

The agreement with the high redshift ($3.6 \leq z \leq 5.0$) results of Fan et al. (2001) is very good in shape, although somewhat discrepant in normalization. Because of their small sample size, Fan et al. (2001) used a single power-law fit to the QLF, but found that the best-fit slope ($\alpha = -2.58 \pm 0.23$) was significantly flatter than at low redshift, suggesting strong evolution was present in the bright-end slope of the QLF. Because of this, the agreement with our results is, at first glance, surprising, as we do not allow for evolution in the slopes α and β , but can be explained by the fast evolution we find for $M_{*,J}$. At $z > 4$ our sample is not large enough to accurately constrain $M_{*,J}$, but based on the $3 < z < 4$ redshift bin we can rule it out being fainter than $M_{*,J} \approx -28$. Using the color conversion based our slightly reddened AGN SED template to go from J to the 1450\AA magnitude used by Fan et al. (2001), we find that the magnitude break is either within the magnitude range of their sample or brighter than it (see §B.2 for details). Thus, in our best-fit LDE model, the QLF constructed by Fan et al. (2001) is in the transition between the faint and bright ends, naturally explaining their best-fit slope value being in between the low redshift measurements of α and β . We caution the reader, however, that a deeper and larger sample at $z \sim 4$, in

Table 5. Color Transformations for QLF Comparison

QLF	Band X	Color X–J		Mag. System
		E(B–V)=0	E(B–V)=0.05	
Croom et al. (2004)	b_j	1.30	1.45	Vega
Croom et al. (2009)	$g(z = 2)$	–1.16	–0.50	AB
Fan et al. (2001) ^a	1450Å	0.05	0.76	AB
Richards et al. (2006b)	$i(z = 2)$	–1.12	–0.78	AB
Brown et al. (2006)	[8.0]	–6.94	–6.98	Vega
Hopkins et al. (2007)	B	1.29	1.46	Vega

Note. — The color transformations used for the QLF comparisons of §4.3 as derived from our AGN SED template for E(B–V) values of 0 and 0.05. The colors are shown in the AB system for QLF studies using bands with that calibration, while they are shown in Vega otherwise.

^aWolf et al. (2003) and Jiang et al. (2009) use the same band as Fan et al. (2001).

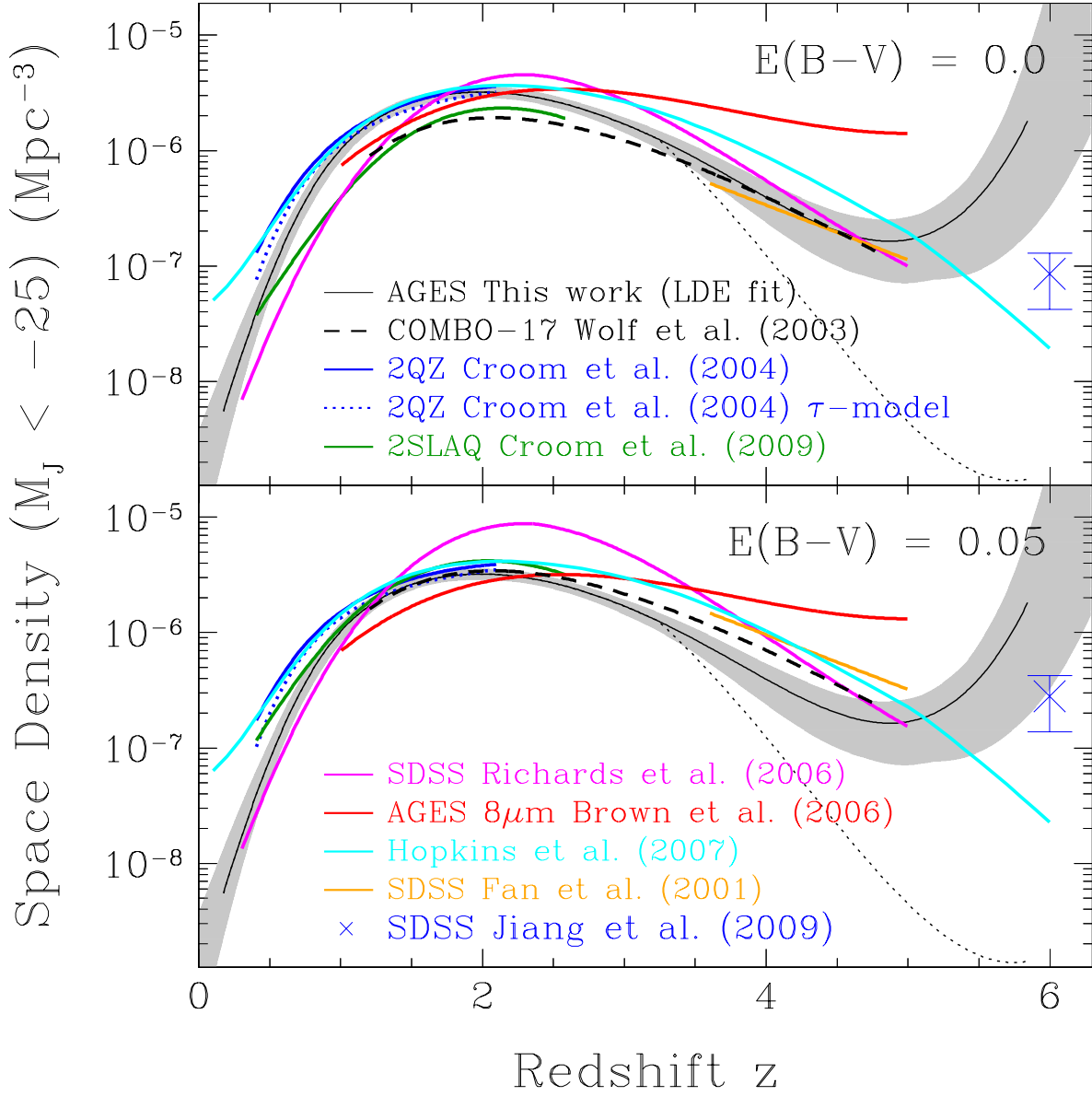


Fig. 15.— Space density of bright quasars as determined from our best-fit LDE model. The upwards turn at $z > 5$ is unlikely to be real (see §B.2 for details). The gray shaded region shows the 2σ ($\Delta\chi^2 \leq 4$) confidence region of our fit. We also show the space density predicted by the studies we discuss in §4.3. We use our AGN template convert between the different bands of each study assuming no reddening (*top*) and $E(B - V) = 0.05$ (*bottom*). The dotted black line shows the space density predicted from the best-fit LDE model but assuming a bright limit for $M_{*,J}(z)$ of -28 .

which the QLF break is clearly visible, is needed to eliminate the model dependence of this result and corroborate our interpretation.

Figures 12 and 13 show, for each study where we could make the comparison, the best fit power-law indices α and β . The agreement between all different studies (including ours) is generally bad, although we note that our estimates for α and β are generally within the range determined by all other studies we show rather than at an extreme.

X-ray surveys have found results that broadly agree with our estimates. In particular, Hasinger et al. (2005) found that the soft X-ray luminosity function (SXLf) of AGNs between $0 < z < 4.8$ is well described by a double power-law functional form allowing for luminosity dependent density evolution (LDDE). Recently, Aird et al. (2010) found that the 2 – 10 keV luminosity function of AGNs between $0 < z < 3.5$ is equally well described by an LDDE model and by a simpler combination of just luminosity and density evolution, similar to our LDE model. While we cannot directly compare our results to these X-ray luminosity functions because our AGN SED template does not extend into this wavelength regime, the general trends agree in that the evolution of the QLF must be in both luminosity and density.

4.4. Comparison with the IRAC-selected QLF

In §3.1 we argue that the selection criteria used to target AGNs by their IRAC colors, which consists of slight modifications of the Stern et al. (2005) criterion, are subject to two strong biases, namely losing AGNs that are faint in comparison to their host galaxies and in the redshift range $4 < z < 5$. In this section, we compare the AGN luminosity function derived in the previous sections and that constructed by considering only the IRAC selected objects. Figure 16 shows the host-corrected IRAC-only QLF along with its corresponding best-fit LDE, PLE and PDE models. The best-fit models are also summarized in Table 6. Note that there are no IRAC-selected AGNs in the lowest redshift range ($z < 0.15$).

In general, the IRAC-selected QLF has a significantly flatter faint end slope β than that of our full sample. This is consistent with Figure 9, where we show that intrinsically fainter AGN typically have larger $L_{\text{Host}}/L_{\text{AGN}}$ ratios because the method is only sensitive to objects whose mid-IR colors are dominated by the AGN rather than by the host. Although the minimum $L_{\text{AGN}}/L_{\text{Host}}$ ratio for selection is dependent on the source’s redshift, the AGN’s reddening and the spectral type of the host, it roughly corresponds to requiring $L_{\text{AGN}}/L_{\text{Host}} \gtrsim 1$. Since lower L_{AGN} sources tend to have lower values of $L_{\text{AGN}}/L_{\text{Host}}$, the IRAC selection criteria eliminates more faint than bright AGNs from our sample. Few faint AGNs are selected by their IRAC colors, even though the region is well populated by the MIPS and

Table 6. IRAC Selected Host Corrected J-band QSO Luminosity Function Parametric Fits

Parameter	LDE	PLE	PDE
χ^2	57	143	154
χ^2_{ν}	1.427	3.254	3.571
α	-3.29 ± 0.05	-3.29 ± 0.05	-3.29 ± 0.05
β	-1.11 ± 0.07	-1.16 ± 0.06	-1.40 ± 0.04
$M_{*,J}$	-26.03 ± 0.15
$M_{*,J}(z_1)$	-23.56 ± 0.21	-23.81 ± 0.18	...
$M_{*,J}(z_2)$	-24.84 ± 0.14	-24.99 ± 0.14	...
$M_{*,J}(z_3)$	-26.07 ± 0.13	-25.80 ± 0.14	...
$M_{*,J}(z_4)$	-30.11 ± 0.77	-15.74 ± 2.01	...
$\log \phi_*(0)^a$...	-4.97 ± 0.05	...
$\log \phi_*(z_1)$	-4.81 ± 0.12	...	-5.91 ± 0.13
$\log \phi_*(z_2)$	-4.86 ± 0.08	...	-5.71 ± 0.10
$\log \phi_*(z_3)$	-4.89 ± 0.06	...	-5.38 ± 0.07
$\log \phi_*(z_4)$	-5.04 ± 0.06	...	-5.16 ± 0.06
$\log \phi_*(z_5)$	-6.72 ± 0.15	...	-6.28 ± 0.17
$M_{*,J}(0)$	-21.52	-22.38	...
k_1	2.01	1.20	...
k_2	-0.81	-0.05	...
k_3	0.13	-0.10	...

Note. — The best fit parameters of each of our three models for the QLF with the formal 1σ error-bars from the Levenberg – Marquardt fitting algorithm. For an easier comparison with other results in literature, we also show the values of the parameters of the more commonly used functional form for the evolution of M_* shown in equation (5). We show no error-bars for this values as correlations between them can be highly significant.

^a $h^3 \text{ Mpc}^{-3} \text{ mag}^{-1}$

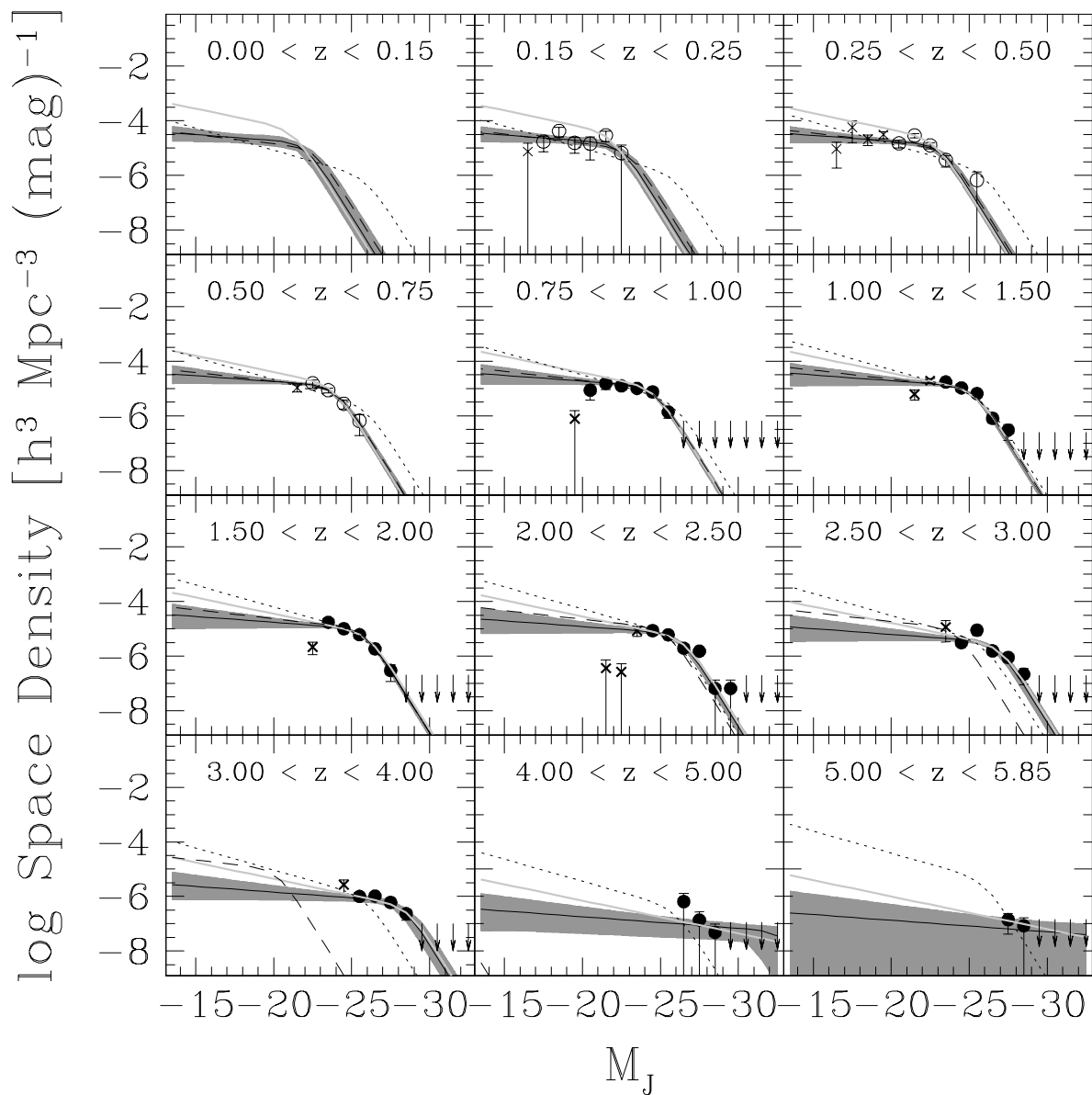


Fig. 16.— Same as Figure 7 but constructed only from IRAC selected sources. For reference, the solid light gray line shows the best-fit LDE model to the full sample (see Fig. 7).

X-ray selected AGNs.

Figure 14 shows the evolution of $M_{*,J}(z)$ and $\log[\phi_*(z)]$ along with those of our full sample. The evolution of the $M_{*,J}$ parameter is largely unaffected by the biases of the IRAC AGN selection, but the evolution of the $\log[\phi_*(z)]$ is qualitatively different at low redshifts ($z < 1$). While for the full sample $\log[\phi_*(z)]$ increases strongly with decreasing redshift, for the IRAC selected sample it is flat. This is consistent with our discussion of the flatter faint end slope. Although the effects of the IRAC selection biases have a stronger effect upon lower luminosity objects, at $z < 1$ they still affect the space density estimate for AGNs of magnitude $M_{*,J}(z)$ with some significance. However, since $M_{*,J}(z)$ becomes brighter with increasing redshift, at $z > 1$ the IRAC selection biases have little effect on the estimated space density of objects brighter than the characteristic magnitude $M_{*,J}(z)$.

5. Conclusions

We derived the J -band QSO luminosity function both with and without the flux contribution of the host galaxy, using 1838 mid-IR and X-ray selected AGN in the redshift range $0 < z < 5.85$. Our sample is based upon the multi-wavelength photometry of the NDWFS survey and the spectroscopic follow up of IRAC selected objects by AGES. We used the set of low resolution SED templates for galaxies and AGNs presented in a previous paper (Paper I) to accurately characterize the properties of the selection function and take them into account when building the QSO luminosity function (QLF). The IRAC color selection of sources by the AGES survey used variations of the Stern et al. (2005) selection criteria. Based on our AGN SED template, such selection criteria are biased towards high Eddington ratio objects so that mid-IR colors are dominated by the AGN, and against redshifts near $4 \lesssim z \lesssim 5$ where the mid-IR color tracks make a “blue loop” outside the color selection region due to $H\alpha$ emission redshifted into the [3.6] IRAC channel. Our IRAC-selected sample contains few objects in this redshift range (see Figure 3) relative to both higher and lower redshifts. Including MIPS and X-ray selected sources largely solves these problems.

Using our low resolution templates we have corrected the objects for host contamination and have also estimated the bolometric QLF of our sources. Our host corrected luminosity functions show that the space density of bright AGN strongly decreases from $z = 3$ to $z = 0$. The best-fit model to the LF suggests that, in contrast, the space density of faint quasars is relatively constant in this redshift range. While the data is consistent with this behavior, it is not strongly constraining. The redshift at which this steep decline begins is also a strong function of luminosity. At $z > 3$ we observe a decrease in the space density of AGNs at all luminosities.

We have modeled the QLF by a double power-law with redshift independent slopes. Because of our modest sample volume, the bright-end slope (α) cannot be well constrained, and we imposed a prior based on the value measured by Croom et al. (2004) with the 2QZ survey. Pure luminosity (PLE) and pure density evolution (PDE) fail to describe the evolution of the QLF over the whole redshift range of our sample. A combination of both is needed to explain the evolution of the QLF with cosmic time. Our combined evolution model (LDE) yields a significantly better fit than either the PLE or PDE models. This is in agreement with measurements of the QLF by Croom et al. (2009) and of the X-ray luminosity function (XLF) by Aird et al. (2010). Our results agree relatively well with other measurements at all redshifts. In particular, we find good agreement with the results of low and high redshift optically selected QLFs and with other measurements that link both redshift ranges. While our fits do not allow for an evolving bright-end slope, we still find good agreement with the $3 < z < 5$ measurements of Fan et al. (2001) and provide a tentative explanation for the flattening of the bright-end slope they find, although we note that a deeper sample is needed to corroborate it. Because our sample does not suffer from the incompleteness of optical selection methods at $2.5 \lesssim z \lesssim 3.5$ it provides an accurate link between low and high redshift QLFs despite the comparatively lower number of objects used.

Finally, we have estimated the QLF using only the IRAC selected AGNs in order to understand the impact of the IRAC selection biases upon the best fit QLF. We find a significantly flatter faint end slope β in comparison to our full sample and a flatter evolution of ϕ_* at $z < 1$. However, at $z > 1$ we find that ϕ_* is generally in good agreement with the estimates obtained using the full sample, and that $M_{*,J}$ is not significantly affected by the biases of the IRAC selection in the full redshift range of our sample.

We would like to thank all the people in the NDWFS, FLAMEX and SDWFS collaborations that did not directly participate in this work. We also thank the anonymous referee for comments and suggestions that helped improve this work. Support for MB was provided by the W. M. Keck Foundation. The work of DS was carried out at Jet Propulsion Laboratory, California Institute of Technology, under a contract with NASA. The AGES observations were obtained at the MMT Observatory, a joint facility of the Smithsonian Institution and the University of Arizona. This work made use of images and/or data products provided by the NOAO Deep Wide-Field Survey (Jannuzi & Dey 1999; Jannuzi et al. in prep.; Dey et al. in prep.), which is supported by the National Optical Astronomy Observatory (NOAO). This research draws upon data provided by Dr. Buell Jannuzi and Dr. Arjun Dey as distributed by the NOAO Science Archive. NOAO is operated by AURA, Inc., under a cooperative agreement with the National Science Foundation.

A. Detection probability of X-ray sources

In §4.1 we discussed our implementation of the Page & Carrera (2000) method for estimating V/V_{\max} (see eqn. [1]). This implementation depends upon the probability that a given object, at a certain redshift z and with a certain magnitude M_J , is included in the sample. For the IRAC and MIPS selection criteria, the detection probability is either 0 or 1, depending on whether the object passes the different color and magnitude cuts. This implicitly assumes that the errors in the measurements are fractionally small, which is sensible for the UV to mid-IR photometry, as the photometric catalogs from which they were selected are typically much deeper than the spectroscopic sample we use. This is not true for the X-ray selected sample. Most sources in the XBoötes survey are detected with only a few counts, and hence the full Poisson probability distribution of their errors must be considered.

To determine the X-ray detection probability of our sources as a function of redshift and J -band absolute magnitude, we use the following procedure. Consider an object located at redshift z_0 with J -band absolute magnitude $M_{J,0}$ and detected with N_0 X-ray counts. The probability that we could have detected it with N_D counts if located at an arbitrary redshift z with an arbitrary absolute magnitude M_J can be expressed as

$$P(N_D|N_0, z, M_J) = \int_0^\infty P[N_D|N(N_T, z, M_J)] P(N_T|N_0) dN_T, \quad (\text{A1})$$

where N_T is the source’s “true” number of X-ray counts at redshift z_0 and absolute magnitude $M_{J,0}$ and $N(N_T, z, M_J)$ is the expected number of counts at redshift z and absolute magnitude M_J . This can be re-written as

$$P(N_D|N_0, z, M_J) \propto \int_0^\infty P[N_D|N(N_T, z, M_J)] P(N_0|N_T) P(N_T) dN_T, \quad (\text{A2})$$

and now both terms, $P[N_D|N(N_T, z, M_J)]$ and $P(N_0|N_T)$, are given by Poisson distributions. The probability of observing objects with N_T X-ray counts is proportional to the number of sources with this intrinsic number of counts. Kenter et al. (2005) determined for the XBoötes survey that the number of sources per unit flux, n_S , is well described by a broken power-law of the shape

$$n_S \propto \begin{cases} N_T^{-1.74} & N_T \leq N_B \\ N_T^{-2.60} & N_T > N_B \end{cases}, \quad (\text{A3})$$

where $N_B \approx 7$ is the number of counts of the break in the power law distribution. However, Kenter et al. (2005) notes that the flux of the break is very poorly constrained and the 1σ interval of the best-fit value puts it between 3 and 25 counts. Since for large values of N_0 the probability is little affected by the value of the power-law index, we assume that the number

of sources per unit flux is a single power-law $n_S \propto N_T^{-y}$, with $y = 1.74$, corresponding to the faint end of equation A3.

Assuming that all sources have an X-ray spectrum well described by a power law with photon index $\Gamma = 1.7$, and hence $F_\nu \propto \nu^{-\Gamma+1}$, it can be shown that $N(N_T, z, M_J) = f N_T$, where

$$f = \left(\frac{1+z}{1+z_0} \right)^{2-\Gamma} \left[\frac{D_L(z_0)}{D_L(z)} \right]^2 10^{-0.4(M_J - M_{J,0})}. \quad (\text{A4})$$

Substituting in equation A2 and calculating the integral, we find that the probability of observing a source seen to have N_0 counts at redshift z_0 and magnitude $M_{J,0}$ with N_D counts at redshift z and magnitude M_J is

$$P(N_D|N_0, z, M_J) \propto f^{N_D} (1+f)^{y-N_D-N_0-1} \frac{\Gamma(1+N_D+N_0-y)}{\Gamma(1+N_D)\Gamma(1+N_0)}, \quad (\text{A5})$$

where $\Gamma(x)$ corresponds to the Γ function. Finally, the probability of a given object detected with N_0 counts at $z = z_0$ and magnitude M_J producing 4 or more counts when located at redshift z and with J -band absolute magnitude M_J is given by

$$P_{det} = \sum_{N_D=4}^{\infty} c(N_D) P(N_D|N_0, z, M_J) \bigg/ \sum_{N_D=0}^{\infty} P(N_D|N_0, z, M_J), \quad (\text{A6})$$

where $c(N_D)$ is the completeness of sources with N_D counts in XBoötes as determined by Kenter et al. (2005).

Note that we have assumed here that the X-ray flux scales linearly with changes in the J -band flux for each object. The X-ray to optical flux ratio (α_{ox}) of AGNs is known to scale with their rest-frame, unreddened, UV flux, but this dependence is weak (Strateva et al. 2005). However, since the changes in M_J for estimating V/V_{max} are small ($\lesssim 1$ mag), assuming strict linearity for scaling the X-ray fluxes instead of a more complex relation does not affect our results.

B. Detailed Comparison with Other QLF Studies

In this section we present a detailed comparison of our results to those of other studies discussed broadly in §4.3. For simplicity, we have divided the different studies according to the properties of their samples into those based on optically selected low redshift samples (Croom et al. 2004, 2009), based on optically selected high redshift samples (Fan et al. 2001; Jiang et al. 2009), those with samples spanning broad redshift ranges (Wolf et al. 2003; Richards et al. 2006b; Brown et al. 2006; Hopkins et al. 2007) and those based on X-ray observations (Hasinger et al. 2005; Aird et al. 2010).

B.1. Optically Selected, Low Redshift QLFs

Croom et al. (2004) combined the observations of the 2dF QSO Redshift Survey (2QZ) and the 6dF QSO Redshift Survey (6QZ) to study the optical (b_j band) QSO luminosity function in the redshift range between 0.4 and 2.1 up to a magnitude limit of $b_j = 20.85$. This corresponds to $I = 20.47$ for our AGN template with no reddening. The low redshift limit of 0.4 was chosen to avoid dealing with extended sources, while the upper limit of 2.1 was chosen because of selection incompleteness caused by stars and the limits of the UVX targeting method employed (Smith et al. 2005). Their full sample consists of 21222 QSOs, most of which are brighter than the break magnitude because of the bright limiting magnitudes. This means that their measurement of the bright-end slope is very precise, while their constraints for the faint end are weak. They parametrize the QLF using the double power-law of equation (3) and assume pure luminosity evolution described using either an exponential scaling of L_* with look-back time defined by an e-folding time (the τ -model), or by a second order polynomial (eqn. [5]). While both fits to their data are acceptable, the τ -model is better. Figure 15 shows, for both models, the space density of bright quasars ($M_J < -26$) as a function of redshift. Both of their parametrizations predict a space density of bright quasars in agreement with our best-fit models at $z \simeq 2$, close to the peak in bright quasar activity. Below $z \simeq 1$, however, they significantly overpredict the number of bright quasars compared to our estimate. Our sample contains few objects with $M_J < -26$ and $z < 1$ (see Figure 7) and so this difference may not be highly significant. By construction, our values of α agree very well with those of their polynomial fit (see §4.1), while our values of β disagree at the $\sim 2 - 3\sigma$ level.

Croom et al. (2009) studied the QLF in the $M_g(z = 2)$ band (absolute rest-frame g -band K -corrected to $z = 2$) between $0.4 < z < 2.6$ using spectroscopic observations of optically selected QSOS from the 2SLAQ survey combined with the low redshift part of the SDSS QSO sample of Richards et al. (2006b, discussed later in this section). Their sample contains 15073 QSOs, is limited to objects with $g < 21.85$ and is corrected for host galaxy contamination using statistical relations between the host and quasar luminosities and redshift. They find strong signs of down-sizing and determine that the best-fit functional form for their sample is given by a combined luminosity and density evolution model, similar to our LDE fit, but allowing α to evolve and limiting the $M_{*,g}(z)$ and $\log[\phi_*(z)]$ polynomials to second order in z (see eqns. [4] and [6]). Their sample cannot be well fit by simple PLE or PDE models, in agreement with our results (see §4.2). Figure 12 shows their best-fit values of α , as a function of redshift, and β . Between $1 < z < 2$, their α agrees relatively well ($< 3\sigma$) with our best-fit LDE parameter, but at higher and lower redshift it is significantly different. On the other hand, β agrees very well with our LDE estimate. For completeness, we show the values of α and β estimated by Richards et al. (2005) using an earlier version of

the 2SLAQ data set. Richards et al. (2005) assumed the same model and best-fit parameter values of Croom et al. (2004) and used the 2SLAQ QLFs to only fit β , which is the only unreliable value of the 2QZ survey results. The estimate of β by Richards et al. (2005) agrees well with ours (the combination of both parameters is $\sim 1.5\sigma$ different than our estimates). In Figure 15 we show the predicted space density of bright quasars, and when considering the slightly reddened AGN templates, the agreement is very good over the whole redshift range.

B.2. Optically Selected, High Redshift QLFs

High redshift quasars ($z > 3$) are found by different color selection methods and are generally fit as a separate population. Fan et al. (2001) used a sample of 39 SDSS QSOs with $i < 20$ selected by their observed optical colors and spanning $3.6 < z < 5.0$ to study the rest-frame 1450Å QLF. Because their sample is not very deep and contains few objects, they model the QLF by a single power-law with pure luminosity evolution. They divided their sample into three redshift bins with edges of 3.3, 3.9, 4.4 and 5.0, and either two or three luminosity bins at each redshift. Their results show a bright-end slope of -2.58 ± 0.23 (see Figure 13), which is considerably shallower than the value of ≈ -3.31 found by Croom et al. (2004) using the 2QZ survey for low redshifts. This argues for a strong evolution of the bright-end slope of the QLF. Nonetheless our best-fit LDE model is not inconsistent with the results of Fan et al. (2001), despite the fact that we do not allow for evolution in α or β . The evolution of $M_{*,J}$ we find is fast enough to suggest that the magnitude bins spanned by their sample likely fall in the transition region between the bright and faint ends of the QLF. If we use our AGN template (with a reddening of 0.05 mags) to transform our estimates of $M_{*,J}$ into $M_{*,1450}$ at each of their redshift bins, we obtain $M_{*,1450} = (-28.19, -30.36, -34.88)$ for $z = (3.75, 4.15, 4.7)$, all fainter than the objects used in their sample (see Figure 1 of Fan et al. 2001), arguing that their objects are in the faint end of the QLF. Note, however, that our constraints on M_* at $z > 4$ are weak, although the absence of very bright quasars leads to strong lower bounds on $M_{*,J}$. At $z = 3.75$ our data rules out an $M_{*,J}$ significantly fainter than -28 (see Fig. 7) which corresponds to $M_{*,1450} = -26.35$ and falls within the magnitude range of the Fan et al. (2001) sample ($-27.5 < M_{1450} < -25.5$). In other words, the fast evolution in M_* suggested by our sample gives a natural explanation to the observed flattening of α . Figure 15 shows the predicted space density of bright quasars from the study of Fan et al. (2001). The agreement is good over their whole redshift range when using the unreddened templates to convert the M_J limit into 1450Å, but somewhat discrepant in normalization, but not shape, for the reddened template. This discrepancy is probably not very significant due to the small number of objects that comprise their sample.

Jiang et al. (2009) studied the high redshift 1450Å QLF from a combined sample of 27 quasars at $z \sim 6$ with a limiting magnitude of 21.8 in z -band. The QLF of their sample is well described by a single power-law with index -2.6 ± 0.3 , shown in Figure 13, consistent with the redshift $z \sim 3$ QLF of Fan et al. (2001). The M_{1450} absolute magnitude range of their sample ($-28 \lesssim M_{1450} \lesssim -25$) is similar to that of the Fan et al. (2001) sample, and hence the same caveats with regards to the change in the bright-end slope at high redshifts apply. In Figure 15 we show the predicted space density compared to that of our favored fitting model. Our results significantly overpredict the number of bright quasars as compared to Jiang et al. (2009), however this may be due simply to our inability to constrain $M_{*,J}$ at $z \sim 6$ (see discussion in previous paragraph). The same Figure shows the predicted space density if we assume a bright limit of $M_{*,J} = -28$ for our fits, and in that case we severely underestimate the space density of bright quasars in comparison to Jiang et al. (2009). Since the real case likely lies between this lower bound and the value estimated from our fits, this discrepancy is unlikely to be significant.

B.3. Broad Redshift Range QLFs

There have been several earlier attempts to construct the QLF on both sides of the peak density at $z \sim 2.1$. Wolf et al. (2003) studied the rest-frame UV (1450Å) luminosity function of 192 quasars from the COMBO-17 survey (0.78 deg²) in the redshift range $1.2 < z < 4.5$. This survey used a combination of 17 narrow, medium and broad bands to securely identify quasars over this redshift range and determine photometric redshifts. The lower redshift limit was chosen to avoid dealing with host galaxy contamination to the SED, while the higher limit was chosen to eliminate 3 bright QSOs whose existence was grossly inconsistent with their lower redshift predictions and predictions from other studies. Their sample was equally well described by pure luminosity and pure density evolution and they did not use a combined evolution model. The parametric form chosen by Wolf et al. (2003) is a polynomial in $\log \phi$, and so we cannot directly compare model parameters. However, we can compare the expected space density of bright quasars, which is shown in Figure 15 for their pure density evolution model. The predicted redshift for the peak of the bright quasars density is $z_{peak} = 2.08$, consistent with the value we find of $z_{peak} = 2.0 \pm 0.1$ (2σ error bars). The agreement is good at all redshifts, given the small number of quasars in the sample of Wolf et al. (2003), regardless of the reddening value assumed for our AGN template.

Richards et al. (2006b) also measured the QLF evolution from low to high redshift. Using a sample of 15343 SDSS QSOs detected in 1622 deg² to measure the redshift 2 i -band (i -band K-corrected to $z = 2$) QSO luminosity function between $0.3 < z < 5.0$ up to a

limiting observed magnitude of $i = 19.1$ for $z < 3$ and $i = 20.2$ for $z > 5$. These limits correspond to $I < 18.6$ and $I < 19.7$ respectively for our unreddened AGN template. Their sample was selected by optical colors and by radio emission from the FIRST survey. Because of the optical color selection, their sample is very incomplete at redshifts between ~ 2.5 and ~ 3 , although this is partially alleviated by the inclusion of the radio sources. Because of the shallowness of their survey, Richards et al. (2006b) chose to model the QLF as a single power-law. They assume a pure luminosity evolution model since a single power-law description of the QLF cannot separate the effects of density and luminosity evolution. They also allow for the bright-end power-law index to evolve after redshift 2.4, as it is strongly favored by their data. As shown in Figure 15, our prediction for the number of bright quasars as a function of redshift agrees generally well with that of Richards et al. (2006b) at low redshift when the reddened AGN template is used to convert between magnitudes. At $z \sim 2$, however, the agreement is relatively poor, significantly higher than our prediction. However, because their sample is a subset of the Croom et al. (2009) sample, and their predictions agree very well with ours in this redshift range, this is unlikely to be very significant. At higher redshift the differences in predictions decrease significantly and agree very well at $z \sim 5$.

Brown et al. (2006) studied the [8.0] luminosity function using a sample of 183 MIPS $24\mu\text{m}$ selected QSOs brighter than 1mJy with redshifts between 1 and 5 taken from an earlier release of the AGES survey. Brown et al. (2006) did not include objects with $z < 1$ in order to avoid complications with the spectroscopic completeness for extended sources. They fit their luminosity function with a single power-law and assumed pure luminosity evolution using the same redshift polynomial we considered here (although in the form of eqn. [5]). They find a value of $\alpha = -2.75$, much shallower than our bright slope. This is not unexpected, as their sample has sources from both sides of the magnitude break, but it is too small to fit α and β independently. Figure 15 shows the evolution of the space density of bright quasars determined by Brown et al. (2006). The space density we determine peaks at $z_{\text{peak}} = 2.0 \pm 0.1$, well below the peak at $z_{\text{peak}} = 2.6 \pm 0.3$ found by Brown et al. (2006) although only $2\text{-}\sigma$ discrepant. The predicted number of bright quasars from their best-fit functional form roughly agrees with that of our best-fit model at $z \lesssim 3$, but the agreement is more discrepant at higher redshifts. The discrepancies are, however, not very significant due to the small number of objects that went into building this sample.

In this context, it is worth noting the work of Hopkins et al. (2007), who studied the evolution of the bolometric QLF from $z \sim 0$ and $z \sim 6$ from a compilation of observed binned QLFs from many surveys in the literature across many wavelengths, from X-ray to $15\mu\text{m}$ (see their Table 1 for a list of all surveys used). A detailed treatment of reddening and the AGN SED was done in order to combine all the samples accordingly, although the required assumptions may introduce systematic errors into their final results. Hopkins et al. (2007)

found the resulting bolometric QLF was best described by a double power-law (eqn. [3]) with evolution in the characteristic bolometric luminosity (of a different form than that we assume), and in the slopes α and β . Figure 13 shows the values of the latter two parameters as a function of redshift. At $z = 0$, both α and β are highly discrepant with most other measurements. The value of β at low redshifts is much lower than our LDE fit and all other literature measurements we present here, but agrees well with the value from our PLE and PDE fits. However, α is still inconsistent at the 3σ level from them. At $z = 1$, the combination of both parameters coincide at the 3σ level well with those determined from our LDE fit, where α is more similar than β . At higher z , the value of β is roughly consistent with that of our LDE fit, but the value of α is lower by a very significant amount. Figure 15 shows the prediction of their best-fit functional form for the density of bright quasars. We have incorporated their results into this plot by using the C routine `qlf_calculator` provided by Hopkins et al. (2007) to generate B-band luminosity functions. The prediction is generally above that of our best-fit functional form, but seems to agree at $z \sim 2$. Their best-fit model predicts a density peak at $z_{\text{peak}} = 2.14$, consistent with our estimate of $z_{\text{peak}} = 2.0 \pm 0.1$ at about 3σ . At lower z , their functional form overpredicts the number of bright QSOs relative to our results but is consistent with the results of Croom et al. (2004). This is not highly surprising, as the 2QZ survey sample is a subset of the data used by Hopkins et al. (2007).

B.4. X-ray QLFs

X-ray surveys have found results that broadly agree with our measurements of the QLF, although we cannot directly compare them with our results as our templates do not extend into the X-ray regime. In particular, Hasinger et al. (2005) studied the soft X-ray luminosity function (SXLF) between $0 < z < 4.8$ with a combined sample from several ROSAT, XMM-*Newton* and *Chandra* surveys. The different samples are limited to relatively bright X-ray fluxes in order to minimize incompleteness in the redshift measurements. Because of this, their sample does not provide very good constraints on the faint end of the SXLF. Hasinger et al. (2005) found that the evolution of the SXLF is not well described by pure luminosity evolution, but is well fit by a luminosity-dependent density evolution (LDDE) model. This LDDE model is not similar to any of the models we discuss in our sample, however Croom et al. (2009) finds that their 2SLAQ and SDSS combined optical sample is better described by a combination of luminosity and density evolution rather than by an LDDE model. The analysis of Hasinger et al. (2005) shows that the evolution of low luminosity AGNs is qualitatively different than that of brighter AGNs, similar to our results (see §4.2 and Figure 8). They find that the space density of AGNs peaks at lower redshifts for fainter objects than for brighter ones, but also that it starts declining at lower redshifts

for fainter AGNs, unlike what we see in Figure 8.

Recently, Aird et al. (2010) studied the 2 – 10 keV X-ray luminosity function (XLF) between redshifts $0 < z < 3.5$ from a combined sample of the *Chandra* Deep Field North and South surveys, the AEGIS-X survey, the *ASCA* Large Sky and Medium Sensitivity surveys and other smaller surveys. To minimize the problems of optical spectroscopic identification of the X-ray sources, they used a combination of spectroscopic and photometric redshifts. Their sample is composed of low redshift hard X-ray selected objects (limited to $z < 1.2$ to minimize the effects of catastrophic photometric redshift errors) and of high redshift objects ($z \gtrsim 2$) selected by a combination of soft X-ray detection and optical colors. To build the XLF, they used a Bayesian approach to account for errors in the X-ray flux measurements and photometric redshifts of their sources, as well as the Eddington bias, in combination with detailed modeling of their selection functions. Aird et al. (2010) find that their sample is equally well described by an LDDE model and by a combination of luminosity and density evolution, similar to our LDE model but with a different parametrization. They also find that the space density of faint AGNs evolves differently than that of brighter objects, however the redshift of the peak of AGN activity shifts much more weakly with luminosity than found by Hasinger et al. (2005) and other XLF studies. They also find that the decline to higher redshifts is much weaker than those found by other XLF studies.

REFERENCES

- Aird, J., et al. 2010, MNRAS, 401, 2531
- Antonucci, R. 1993, ARA&A, 31, 473
- Ashby, M. L. N., et al. 2009, ApJ, 701, 428
- Assef, R.J., Kochanek, C.S., Brodwin, M., Brown, M. J. I., Caldwell, N., Cool, R. J., Eisenhardt, P., Eisenstein, D., Gonzalez, A. H., Jannuzi, B. T., Jones, C., McKenzie, E., Murray, S. S., Stern, D. 2008, ApJ, 676, 286
- Assef, R. J., et al. 2010, ApJ, 713, 970
- Baldwin, J. A., Phillips, M. M., & Terlevich, R. 1981, PASP, 93, 5
- Bertin, E. & Arnouts, S. 1996, A&AS, 117, 393
- Bower, R. G., Benson, A. J., Malbon, R., Helly, J. C., Frenk, C. S., Baugh, C. M., Cole, S., & Lacey, C. G. 2006, MNRAS, 370, 645

- Brand, K., et al. 2006, *ApJ*, 641, 140
- Brown, M.J.I. et al. 2006, *ApJ*, 638, 88
- Cole, S., et al. 2001, *MNRAS*, 326, 255
- Cool, R. J. 2010, in preparation.
- Cool, R. J. 2007, *ApJS*, 169, 21
- Cool, R. J., et al. 2006, *AJ*, 132, 823
- Croom, S.M., et al. 2004, *MNRAS*, 349, 1397
- Croom, S. M., et al. 2009, *MNRAS*, 399, 1755
- Croton, D. J., et al. 2006, *MNRAS*, 365, 11
- Dai, X., et al. 2009, *ApJ*, 697, 506
- Dey, A. et al. 2010, in preparation.
- Di Matteo, T., Springel, V., & Hernquist, L. 2005, *Nature*, 433, 604
- Donley, J. L., Rieke, G. H., Pérez-González, P. G., & Barro, G. 2008, *ApJ*, 687, 111
- Elston, R.J., Gonzalez, A. H. et al. 2006, *ApJ*, 639, 816
- Efstathiou, G., Ellis, R. S., & Peterson, B. A. 1988, *MNRAS*, 232, 431
- Fabricant, D., et al. 2005, *PASP*, 117, 1411
- Fan, X. 1999, *AJ*, 117, 2528
- Fan, X., et al. 2001, *AJ*, 121, 54
- Fazio, G. G., et al. 2004, *ApJS*, 154, 10
- Gorjian, V., et al. 2008, *ApJ*, 679, 1040
- Hasinger, G., Miyaji, T., & Schmidt, M. 2005, *A&A*, 441, 417
- Hopkins, P. F., Hickox, R., Quataert, E., & Hernquist, L. 2009, *MNRAS*, 398, 333
- Hopkins, P. F., Richards, G. T., & Hernquist, L. 2007, *ApJ*, 654, 731

- Hopkins, P. F., Hernquist, L., Cox, T. J., Di Matteo, T., Robertson, B., & Springel, V. 2006, *ApJS*, 163, 1
- Hopkins, P. F., Hernquist, L., Cox, T. J., Di Matteo, T., Martini, P., Robertson, B., & Springel, V. 2005, *ApJ*, 630, 705
- Hopkins, P. F., Hernquist, L., Cox, T. J., Di Matteo, T., Robertson, B., & Springel, V. 2005, *ApJ*, 630, 716
- Kewley, L. J., Dopita, M. A., Sutherland, R. S., Heisler, C. A., & Trevena, J. 2001, *ApJ*, 556, 121
- Jannuzi, B. T. & Dey, A. 1999, *ASP Conference Series*, Vol. 191, p. 111
- Jannuzi, B.T. et al. 2010, in preparation.
- Jiang, L., et al. 2009, *AJ*, 138, 305
- Kauffmann, G., et al. 2003, *MNRAS*, 346, 1055
- Kenter, A., et al. 2005, *ApJS*, 161, 9
- Kochanek, C.S. et al. in preparation
- Lacy, M., et al. 2004, *ApJS*, 154, 166
- Lin, H., Kirshner, R.P., Shectman, S.A., Landy, S.D., Oemler, A., Tucker, D.L. & Schechter, P. L. 1996, *ApJ*, 464, 60
- Martin, D.C. et al. 2005, *ApJ*, 619L, 1
- Miyaji, T., Hasinger, G., & Schmidt, M. 2001, *A&A*, 369, 49
- Morrissey, P., et al. 2007, *ApJS*, 173, 682
- Moustakas et al. 2009, in prep.
- Murray, S.S. et al. 2005, *ApJS*, 161, 1
- Page, M. J., & Carrera, F. J. 2000, *MNRAS*, 311, 433
- Richards, G. T., et al. 2009, *AJ*, 137, 3884
- Richards, G.T. et al. 2006a, *ApJS*, 166, 470
- Richards, G. T., et al. 2006b, *AJ*, 131, 2766

- Richards, G.T. et al. 2005, MNRAS, 360, 839
- Rieke, G. H., et al. 2004, ApJS, 154, 25
- Rowan-Robinson, M., et al. 2008, MNRAS, 386, 697
- Rujopakarn, W., et al. 2010, ApJ, 718, 1171
- Salvato, M., et al. 2009, ApJ, 690, 1250
- Sandage, A., Tammann, G. A., & Yahil, A. 1979, ApJ, 232, 352
- Schmidt, M. 1968, ApJ, 151, 393
- Smith, R. J., Croom, S. M., Boyle, B. J., Shanks, T., Miller, L., & Loaring, N. S. 2005, MNRAS, 359, 57
- Stern, D., et al. 2007, ApJ, 663, 677
- Stern, D. et al. 2005, ApJ, 631, 163
- Strateva, I. V., Brandt, W. N., Schneider, D. P., Vanden Berk, D. G., & Vignali, C. 2005, AJ, 130, 387
- York D. et al. 2000, AJ, 120, 1579
- Weedman, D.W. et al. 2006, ApJ, 651, 101
- Wolf, C., Wisotzki, L., Borch, A., Dye, S., Kleinheinrich, M., & Meisenheimer, K. 2003, A&A, 408, 499